

Splitting-strategies for arbitrary-order fully mixed finite element discretizations for the Biot equations

Fleurianne Bertrand*

Jakub Wiktor Both†

Tugay Dağlı‡

Abstract

We study the fully-mixed formulation of the Biot equations which is characterized by a symmetric coupling between flow and deformation. This structure enables the use of stable mixed finite elements for each subproblem without strong compatibility condition across the two subphysics. To exploit this flexibility while preserving the conservation structure of both subproblems, we consider fully mixed finite element methods in which the symmetry of the elastic stress tensor is enforced weakly. The resulting mixed formulation exhibits a saddle-point structure whose stability is determined by suitable inf-sup conditions. Inf-sup stability is established for several families of discrete spaces of arbitrary order, leading to optimal a priori error estimates. Iterative splitting strategies, following the classical fixed-stress split with additional tuning are specifically investigated for the fully mixed formulation with proof of convergence and rates depending on the coupling strength. Contrary to previous analyses on coupled problems with symmetric structure, we theoretically prove the efficacy of negative stabilization, consistent with Schur-complement ideas. Numerical results based on analytical solutions and the classical Mandel problem are presented supporting the theory.

Keywords: Biot equations, mixed finite elements, weak symmetry, error analysis, iterative coupling, stabilization

Introduction

The two-way coupling between fluid flow and deformation of porous materials, commonly referred to as poromechanics, is a key component in a wide range of engineering applications, including subsurface energy and storage technologies, geomechanics, biomechanics, and material processing. From a computational viewpoint, poromechanics models exhibit pronounced multi-physics and multi-parameter features, so that robustness with respect to physical parameters and discretization choices, and reliability via error control are central requirements for predictive simulations. This perspective has motivated extensive recent research on stable discretizations, parameter-robust solvers and preconditioners, and adaptive strategies driven by a posteriori error estimates; see, e.g., the overview and motivation in [8] as well as references therein. The most widely used mathematical model in this context is the linear, quasi-static Biot consolidation system [9, 10], which couples mechanical equilibrium of the solid skeleton with mass conservation of the pore fluid. A classical approach is based on a two-field saddle-point formulation in displacement and pore pressure, for which stable conforming finite element choices such as the Taylor–Hood pair yield optimal a priori error estimates under standard assumptions, see [25]. However, a well-known drawback of this formulation is that stability and accuracy may deteriorate in regimes with incompressible constituents, or strongly varying parameters [19], in addition to lack of conservation qualities for mass and linear momentum, prompting the development of alternative formulations designed to be more robust.

A natural remedy is to employ mixed formulations, where additional variables for the Darcy velocity and/or stress are introduced and approximated directly. Moreover, they allow for schemes that honor the conservation properties. As a result, a range of equivalent formulations of the Biot equations exist and have been studied both in terms of discretizations and efficient numerical solution. With a strong focus on the approximation of the flow problem, the three-field formulation of poromechanics, built on a mixed formulation of the flow problem and adding the Darcy velocity as unknown, highlights local mass conservation and introduces a double-saddle point structure; see, e.g., [28, 29]. On the contrary, local conservation of linear momentum can be achieved through a mixed formulation of the elasticity problem, where the symmetry of the total Cauchy stress can be enforced strongly [6] or weakly [18, 5], where for the former the construction of associated approximate function spaces considerably restricts the range of admissible discretizations and increases the computational effort.

*Numerical Analysis of Partial Differential Equations, TU Chemnitz, Germany

†Department of Mathematics, University of Bergen, Norway

‡Numerical Analysis of Partial Differential Equations, TU Chemnitz, Germany

Direct application of both ideas has resulted in poromechanics models with a mixed formulation for the elasticity and converting the saddle-point structure of the elasticity-flow coupling into a symmetric coupling [7] as also highlighted by the underlying gradient flow structure of poromechanics [14]. Finally, fully mixed formulations, combining a mixed approach for both flow and elasticity problems, enable conservation of both mass and linear momentum as well as stronger parameter-robustness of discretizations and solvers [37, 26, 4]. Fully mixed formulations are particularly attractive for a posteriori error estimation since the physically relevant stresses and fluxes are computed directly as primary variables and satisfy local conservation properties. In this setting, Prager–Synge type estimates can be derived by combining the available equilibrated stresses and fluxes with reconstructed kinematically admissible displacement and pressure fields; see, for instance, [3, 2, 30] and the references therein. While the elasticity-flow coupling is symmetric, the underlying subproblems honor a saddle-point structure. A unifying view in connection to the underlying gradient flow structure of poromechanics is presented in [14]. While this observation highlights the flexibility in designing stable spatial discretizations, as long as the subproblems are approximated in a stable manner, this fact has not been exploited and clearly communicated in previous works.

The iterative solution of poromechanics, decoupling flow and elasticity is a common technique and relies on suitable stabilization to ensure unconditional robustness with respect to the coupling strength [22]; direct application of the iterative solver as preconditioner results in parameter robust linear solution [36]. The most popular iterative solver is the fixed-stress split, built on the idea of consecutively solving the flow problem under fixed volumetric stress and followed by solving the elasticity problem with fixed pressure [32]. In the two- and three-field formulation, this physically-motivated scheme results in stabilization of the flow problem [22], while in the five-field formulation it simply results in a naive decoupling [2, 14], which being an alternative minimization is known to converge [13]. Problem-specific analysis has revealed potential to tune convergence properties by a careful choice and optimization of the correct stabilization [24, 15, 33]. For the fully mixed formulation with its symmetric coupling of elasticity and flow, such problem-specific analysis has not yet been presented. We, however, highlight the study of other symmetric problems employing stabilization and in general advocating for (positive) stabilization [27, 16], while intuitively a Schur-complement approach would instead suggest a (negative) destabilization. The latter idea has been successfully applied for an alternative fully dynamic poromechanics model with a symmetric coupling between displacement and flux variables [11], but not for the classical Biot equations.

In this work, we aim to highlight both the flexibility in designing spatial approximations as well as the potential of tuning convergence of the fixed-stress split by careful destabilization (negative stabilization), when considering the five-field formulation of the Biot equations. We show, consistent with the symmetric coupling of the two subproblems as highlighted above, that inf-sup stability of the five-field formulations does not require a compatibility condition across the coupling of flow and deformation, resulting in an entire family of discretization schemes similar to the combination of classical Arnold-Falk-Winther and Raviart-Thomas elements, cf. [2, 4]. In addition, we define a stabilized splitting scheme, iteratively coupling flow and deformation. It is inspired by the fixed-stress split, but suggests negative stabilization L^2 -type. The strength of destabilization is assessed through a theoretical convergence analysis, resulting in a simple expression which is consistent with previous analyses of the two-field formulation [24, 15, 33].

The remainder of the paper is organized as follows. In section 2 and section 3, the fully-mixed formulation of the Biot equations is presented in strong and weak formulation, resembling the five-field formulation with enforced weak symmetry of stress tensors. This structure allows for the use of standard $\mathbb{H}(\text{div}, \Omega)$ -conforming finite element spaces for the stress and Darcy velocity variables and avoids the need for symmetric stress finite element spaces. Based on this framework, we derive families of conforming mixed finite element discretizations of arbitrary order in section 4. In section 5, we investigate the corresponding iterative solution strategies for the resulting coupled saddle-point systems and analyze the behavior of a tuned fixed-stress splitting scheme. Numerical experiments, including tests based on a manufactured solution and the classical Mandel benchmark, illustrate the theoretical findings in section 6. The paper is closed with concluding remarks in section 7.

2 Stress-based porous media equations

We focus on the quasi-static Biot’s model for soil consolidation, where the porous medium is characterized as linearly elastic, homogeneous, isotropic, and filled with a Newtonian fluid [9, 10, 17]. The consolidation process is governed by a system of partial differential equations that integrate the dynamics of the fluid flow with the elastic deformation \mathbf{u} of the solid framework. This elastic problem is based on the reference configuration of the undeformed state described by a domain $\Omega \subset \mathbb{R}^d$ ($d = 2, 3$). The linear elasticity theory implies that the effective stress $\boldsymbol{\theta}$ is related to the strain tensor $\boldsymbol{\varepsilon}(\mathbf{u}) = \frac{1}{2}(\nabla\mathbf{u} + (\nabla\mathbf{u})^\top)$ by the constitutive equation $\boldsymbol{\theta} = 2\mu\boldsymbol{\varepsilon}(\mathbf{u}) + \lambda \text{div}(\mathbf{u})\mathbf{I}$ where λ and μ denote the Lamé coefficients. Considering an external force \mathbf{g} , the equilibrium equation for the porous medium reads

$$-\text{div } \boldsymbol{\theta} + \alpha \nabla p = \mathbf{g} \tag{1}$$

where p denotes the pore pressure and α is the Biot–Willis constant. In the context of mixed finite element methods, it is, however, crucial to consider the equilibrium equation in divergence form. To this end, we introduce the total stress tensor $\underline{\boldsymbol{\sigma}} = \underline{\boldsymbol{\theta}} - \alpha p \underline{\mathbf{I}}$. Since $\nabla p = \text{div}(p \underline{\mathbf{I}})$, note that (1) can now be written as

$$-\text{div } \underline{\boldsymbol{\sigma}} = \mathbf{g} . \quad (2)$$

This will allow us to seek for $\underline{\boldsymbol{\sigma}}$ in $\mathbf{H}(\text{div}, \Omega) = (\mathbf{H}(\text{div}, \Omega))^d$ where $\mathbf{H}(\text{div}, \Omega)$ is the space of vector-valued functions from $\mathbf{L}^2(\Omega)$ that admits a weak divergence in $L^2(\Omega)$. In terms of the total stress, the constitutive relation can be rewritten as

$$\mathcal{A}\underline{\boldsymbol{\sigma}} = \mathcal{A}\underline{\boldsymbol{\theta}} - \mathcal{A}(\alpha p \underline{\mathbf{I}}) = \underline{\boldsymbol{\varepsilon}}(\mathbf{u}) - \frac{\alpha}{2\mu + d\lambda} p \underline{\mathbf{I}} \text{ with } \mathcal{A}\underline{\boldsymbol{\sigma}} := \frac{1}{2\mu} \left(\underline{\boldsymbol{\sigma}} - \frac{\lambda}{2\mu + d\lambda} (\text{tr } \underline{\boldsymbol{\sigma}}) \underline{\mathbf{I}} \right) \quad (3)$$

On the mass conservation side, under a forced fluid extraction or injection process f , the variation of fluid content and the percolation velocity of the fluid $\hat{\mathbf{w}} \in \mathbf{H}(\text{div}, \Omega)$ are related by

$$\frac{\partial}{\partial t} (c_0 p + \alpha \text{div } \mathbf{u}) + \text{div } \hat{\mathbf{w}} = f \quad (4)$$

where c_0 is called storage coefficient. In order to obtain a symmetric variational formulation, it is of interest to reformulate (4) in terms of $\underline{\boldsymbol{\sigma}}$. To this end, note that the constitutive equation implies $\text{tr } \underline{\boldsymbol{\theta}} = (2\mu + d\lambda) \text{div } \mathbf{u}$ such that

$$f = \frac{\partial}{\partial t} (c_0 p + \alpha (\text{tr } \mathcal{A}\underline{\boldsymbol{\theta}})) + \text{div } \hat{\mathbf{w}} = \frac{\partial}{\partial t} (c_0 p + \alpha \text{tr}(\mathcal{A}(\underline{\boldsymbol{\sigma}} + \alpha p \underline{\mathbf{I}}))) + \text{div } \hat{\mathbf{w}} = \frac{\partial}{\partial t} \left(\left(c_0 + \frac{d\alpha^2}{2\mu + d\lambda} \right) p + \frac{\alpha}{2\mu + d\lambda} \text{tr } \underline{\boldsymbol{\sigma}} \right) + \text{div } \hat{\mathbf{w}} .$$

Finally, using the permeability κ , Darcy's law linearly relates the volume flow rate of the fluid to the pressure gradient as follows

$$\hat{\mathbf{w}} = -\kappa \nabla p . \quad (5)$$

Finally, assuming that the boundary is decomposed as $\partial\Omega = \Gamma_f \cup \Gamma_p = \Gamma_t \cup \Gamma_d$. we define

$$\underline{\boldsymbol{\Sigma}}_0 := \{ \underline{\boldsymbol{\tau}} \in H(\text{div}; \Omega)^{d \times d} : \underline{\boldsymbol{\tau}} \cdot \mathbf{n} = 0 \text{ on } \Gamma_t \}, \quad \mathbf{W}_0 := \{ \mathbf{z} \in H(\text{div}; \Omega)^d : \mathbf{z} \cdot \mathbf{n} = 0 \text{ on } \Gamma_f \}.$$

to prescribe the boundary conditions. In order to keep the notation simple, note that we restrict ourselves to homogeneous boundary conditions. The analysis extends in a standard way to non-homogeneous boundary data and the numerical examples presented later employ non-trivial boundary conditions (see subsection 6.2).

In order to focus on the derivation of the mixed formulation of the first-order stress–velocity Biot system and the spatial discretization in the next sections 3 and 4, we employ the commonly used implicit Euler scheme, although any higher-order implicit method could be used without affecting the developments that follow. To this end, let $0 = t_0 \leq t_1 \leq \dots \leq t_N = T$ denote an equidistant partition of the time interval with time step size $\Delta t = t_n - t_{n-1}$, $n = 1, \dots, N \in \mathbf{N}$. Given the data $(\underline{\boldsymbol{\sigma}}^{n-1}, p^{n-1}) \in \underline{\boldsymbol{\Sigma}}_0 \times L^2(\Omega)$ from the previous time level, the time-discrete Biot system at step n reads: Find

$$(\underline{\boldsymbol{\sigma}}, p, \hat{\mathbf{w}}, \mathbf{u}) \in \underline{\boldsymbol{\Sigma}}_0 \times H_{\Gamma_p}^1(\Omega) \times \mathbf{W}_0 \times H_{\Gamma_d}^1(\Omega)^d$$

such that

$$\begin{aligned} -\text{div } \underline{\boldsymbol{\sigma}} &= \mathbf{g} & \text{in } \Omega & & \mathcal{A}\underline{\boldsymbol{\sigma}} &= \underline{\boldsymbol{\varepsilon}}(\mathbf{u}) - \tilde{\alpha} p & \text{in } \Omega & & \underline{\boldsymbol{\varepsilon}}(\mathbf{u}) &= \frac{1}{2} (\nabla \mathbf{u} + (\nabla \mathbf{u})^\top) & \text{in } \Omega \\ \tilde{\alpha} \text{tr}(\underline{\boldsymbol{\sigma}}) + \tilde{c}_0 p + \Delta t \text{div } \hat{\mathbf{w}} &= \tilde{f} & \text{in } \Omega & & \hat{\mathbf{w}} + \kappa \nabla p &= 0 & \text{in } \Omega & & \hat{\mathbf{w}} \cdot \mathbf{n} &= 0 & \text{on } \Gamma_f \\ p &= 0 & \text{on } \Gamma_p & & \underline{\boldsymbol{\sigma}} \cdot \mathbf{n} &= 0 & \text{on } \Gamma_t & & \mathbf{u} &= 0 & \text{on } \Gamma_d. \end{aligned} \quad (6)$$

where

$$\tilde{\alpha} := \frac{\alpha}{2\mu + d\lambda}, \quad \tilde{c}_0 := c_0 + \frac{d\alpha^2}{2\mu + d\lambda}, \quad \tilde{f} := \Delta t f + \tilde{\alpha} \text{tr}(\underline{\boldsymbol{\sigma}}^{n-1}) + \tilde{c}_0 p^{n-1}.$$

3 Derivation of the mixed formulation

It is well known that a variational formulation based on the Hellinger-Reissner principle can be derived from the constitutive equation (3) via the Lagrange multiplier method by eliminating the constraints of equilibrium equations. However, the presence of symmetric gradient $\underline{\varepsilon}(\mathbf{u})$ requires a symmetric test space for the integration by parts when testing this equation with a test stress $\underline{\boldsymbol{\tau}} \in \mathbf{H}(\text{div}, \Omega)$. To avoid later on the construction of a symmetric space, we consider the additional variable $\underline{\boldsymbol{\xi}} = \frac{1}{2} \nabla \times \mathbf{u}$, which is a scalar for $d = 2$ and a vector for $d = 3$. It holds

$$\underline{\varepsilon}(\mathbf{u}) = \nabla \mathbf{u} - \underline{\boldsymbol{\xi}} \cdot \chi,$$

where the matrix $\underline{\boldsymbol{\xi}} \cdot \chi \in \mathbb{R}^{d \times d}$ is defined componentwise by

$$(\underline{\boldsymbol{\xi}} \cdot \chi)_{ij} = \varepsilon_{ij} \xi \text{ if } d = 2, \text{ and } \sum_{k=1}^3 \varepsilon_{ijk} \xi_k \text{ if } d = 3, \quad i, j = 1, \dots, d.$$

with the Levi-Civita symbol ε . The new constitutive equation $\mathcal{A}\underline{\boldsymbol{\sigma}} = \nabla \mathbf{u} - \underline{\boldsymbol{\xi}} \cdot \chi - \tilde{\alpha} p \mathbf{I}$ can now be tested with a non-symmetric test stress $\underline{\boldsymbol{\tau}} \in \mathbf{H}(\text{div}, \Omega)$ to obtain

$$(\mathcal{A}\underline{\boldsymbol{\sigma}}, \underline{\boldsymbol{\tau}}) + (\mathbf{u}, \text{div } \underline{\boldsymbol{\tau}}) + (\underline{\boldsymbol{\xi}} \cdot \chi, \underline{\boldsymbol{\tau}}) + \tilde{\alpha}(p, \text{tr}(\underline{\boldsymbol{\tau}})) = 0 \quad (7)$$

where we have integrated by parts the second term. This now corresponds to the minimization under constraints of $\mathcal{A}\underline{\boldsymbol{\sigma}} = (\mathcal{A}\underline{\boldsymbol{\sigma}}, \underline{\boldsymbol{\tau}})$. Indeed, the Lagrange parameter $\mathbf{u} \in \mathbf{L}^2(\Omega)$ corresponds to the weak form of (1) as it holds

$$-(\text{div } \underline{\boldsymbol{\sigma}}, \mathbf{v}) = (\mathbf{g}, \mathbf{v}) \quad (8)$$

for all $\mathbf{v} \in \mathbf{L}^2(\Omega)$. The Lagrange parameter $\underline{\boldsymbol{\xi}} \in L^{d(d-1)/2}(\Omega)$ corresponds to the symmetry constraint as $\underline{\boldsymbol{\sigma}} = 0$, which in weak form reads

$$(\underline{\boldsymbol{\sigma}}, \underline{\boldsymbol{\eta}} \cdot \chi) = 0 \quad (9)$$

for all $\underline{\boldsymbol{\eta}} \in L^{d(d-1)/2}(\Omega)$. The weak imposition of equilibrium and symmetry is consistent, since divergence and skew-symmetric components of stresses in $\mathbf{H}(\text{div}, \Omega)$ can be prescribed independently. More precisely, for any $(\mathbf{v}, \underline{\boldsymbol{\eta}}) \in \mathbf{L}^2(\Omega) \times L^2(\Omega)^{d(d-1)/2}$ there exists $\underline{\boldsymbol{\tau}} \in \mathbf{H}(\text{div}, \Omega)$ such that

$$\text{div } \underline{\boldsymbol{\tau}} = \mathbf{v}, \quad (\underline{\boldsymbol{\tau}}, \underline{\boldsymbol{\eta}} \cdot \chi) \gtrsim \|\underline{\boldsymbol{\eta}}\|_0^2, \text{ and } \|\underline{\boldsymbol{\tau}}\|_{\mathbf{H}(\text{div}, \Omega)} \lesssim \|\mathbf{v}\|_0 + \|\underline{\boldsymbol{\eta}}\|_0. \quad (10)$$

The remaining Lagrange parameter $p \in L^2(\Omega)$ in (7) arises from the fluid mass conservation equation (4). In fact, testing (4) with $q \in L^2(\Omega)$ leads to

$$\tilde{c}_0(p, q) + \tilde{\alpha}(\text{tr } \underline{\boldsymbol{\sigma}}, q) + \Delta t(\text{div } \hat{\mathbf{w}}, q) = \langle f, q \rangle := \Delta t(f, q) + \tilde{c}_0(p^{n-1}, q) + \tilde{\alpha}(\text{tr } \underline{\boldsymbol{\sigma}}^{n-1}, q) \quad (11)$$

for all $q \in L^2(\Omega)$. This gives rise to the pressure energy

$$\mathcal{A}_p(p, q) = \tilde{c}_0(p, q) .$$

The Lagrange parameter $\hat{\mathbf{w}} \in \mathbf{H}(\text{div}, \Omega)$ in (11) corresponds to the Darcy constraint (5) as it implies

$$\mathcal{A}_{\hat{\mathbf{w}}}(\hat{\mathbf{w}}, \mathbf{z}) := \boldsymbol{\kappa}^{-1}(\hat{\mathbf{w}}, \mathbf{z}) = -(\nabla p, \mathbf{z}) = (p, \text{div } \mathbf{z}) \quad (12)$$

for all $\mathbf{z} \in \mathbf{H}(\text{div}, \Omega)$. We can now combine the equations (7), (12), (8), (9) and (11) to obtain the final continuous variational formulation: seek $(\underline{\boldsymbol{\sigma}}, p, \hat{\mathbf{w}}, \mathbf{u}, \underline{\boldsymbol{\xi}}) \in \mathbf{X} = \mathbf{H}(\text{div}, \Omega) \times L^2(\Omega) \times \mathbf{H}(\text{div}, \Omega) \times \mathbf{L}^2(\Omega) \times (L^2(\Omega))^{2d-3}$ such that

$$\begin{aligned} \mathcal{A}_{\underline{\boldsymbol{\sigma}}}(\underline{\boldsymbol{\sigma}}, \underline{\boldsymbol{\tau}}) + \tilde{\alpha}(p, \text{tr}(\underline{\boldsymbol{\tau}})) + (\mathbf{u}, \text{div } \underline{\boldsymbol{\tau}}) + (\underline{\boldsymbol{\xi}} \cdot \chi, \underline{\boldsymbol{\tau}}) &= 0 \\ \tilde{\alpha}(\text{tr } \underline{\boldsymbol{\sigma}}, q) + \mathcal{A}_p(p, q) + \Delta t(\text{div } \hat{\mathbf{w}}, q) &= \langle \tilde{f}, q \rangle \\ (\text{div } \underline{\boldsymbol{\sigma}}, \mathbf{v}) &= -(\mathbf{g}, \mathbf{v}) \\ (\underline{\boldsymbol{\sigma}}, \underline{\boldsymbol{\eta}} \cdot \chi) &= 0 \\ (p, \text{div } \mathbf{z}) &= -\mathcal{A}_{\hat{\mathbf{w}}}(\hat{\mathbf{w}}, \mathbf{z}) = 0 \end{aligned} \quad (13)$$

for all $(\underline{\boldsymbol{\tau}}, q, \mathbf{z}, \mathbf{v}, \boldsymbol{\eta}) \in \mathbf{X}$. This system can be cast into the following saddle-point problem: seek $\underline{\mathbf{u}} \in \underline{\mathbf{V}}$ and $\mathbf{p} \in \mathbf{Q}$ such that

$$\begin{aligned} \mathcal{A}(\underline{\mathbf{u}}, \underline{\mathbf{v}}) + \mathcal{B}(\underline{\mathbf{v}}, \mathbf{p}) &= \mathcal{F}(\underline{\mathbf{v}}) \\ \mathcal{B}(\underline{\mathbf{u}}, \mathbf{q}) - \mathcal{C}(\mathbf{p}, \mathbf{q}) &= \mathcal{G}(\mathbf{q}) \end{aligned} \quad (14)$$

holds for all $(\underline{\mathbf{v}}, \mathbf{q}) \in \underline{\mathbf{V}} \times \mathbf{Q}$ with

$$\begin{aligned} \mathbf{Q} &= \mathbf{W}_0 \times \mathbf{L}^2(\Omega) \times (L^2(\Omega))^{2d-3}, & \underline{\mathbf{V}} &= \underline{\boldsymbol{\Sigma}}_0 \times L^2(\Omega), \\ \mathcal{A}(\underline{\mathbf{u}}, \underline{\mathbf{v}}) &= \mathcal{A}((\underline{\boldsymbol{\sigma}}, p), (\underline{\boldsymbol{\tau}}, q)) = \mathcal{A}_{\underline{\boldsymbol{\sigma}}}(\underline{\boldsymbol{\sigma}}, \underline{\boldsymbol{\tau}}) + \mathcal{A}_p(p, q) + \tilde{\alpha}(p, \text{tr } \underline{\boldsymbol{\tau}}) + \tilde{\alpha}(q, \text{tr } \underline{\boldsymbol{\sigma}}), & \mathbf{w} &= \Delta t \hat{\mathbf{w}} \\ \mathcal{B}(\underline{\mathbf{v}}, \mathbf{p}) &= \mathcal{B}((\underline{\boldsymbol{\tau}}, q), (\mathbf{w}, \mathbf{u}, \boldsymbol{\xi})) = (q, \text{div } \mathbf{w}) + (\mathbf{u}, \text{div } \underline{\boldsymbol{\tau}}) + (\boldsymbol{\xi} \cdot \boldsymbol{\chi}, \underline{\boldsymbol{\tau}}), & \mathcal{F}(\underline{\mathbf{v}}) &= \mathcal{F}((\underline{\boldsymbol{\tau}}, q)) = \langle \tilde{\mathbf{f}}, q \rangle, \\ \mathcal{C}(\mathbf{p}, \mathbf{q}) &= \mathcal{C}((\mathbf{w}, \mathbf{u}, \boldsymbol{\xi}), (\mathbf{z}, \mathbf{v}, \boldsymbol{\eta})) = \frac{1}{\Delta t} \mathcal{A}_{\hat{\mathbf{w}}}(\mathbf{w}, \mathbf{z}) & \mathcal{G}(\mathbf{q}) &= \mathcal{G}((\mathbf{z}, \mathbf{v}, \boldsymbol{\eta})) = -(\mathbf{g}, \mathbf{v}). \end{aligned} \quad (15)$$

The bilinear form \mathcal{B} encodes the constraint structure of the mixed formulation. Its associated kernel spaces

$$\begin{aligned} H &:= \{\mathbf{p} \in \mathbf{Q} : \mathcal{B}(\underline{\mathbf{v}}, \mathbf{p}) = 0 \ \forall \underline{\mathbf{v}} \in \underline{\mathbf{V}}\} = \{(\mathbf{w}, 0, 0) \in \mathbf{Q} : \text{div } \mathbf{w} = 0\} \\ \text{and } K &:= \{\underline{\mathbf{v}} \in \underline{\mathbf{V}} : \mathcal{B}(\underline{\mathbf{v}}, \mathbf{p}) = 0 \ \forall \mathbf{p} \in \mathbf{Q}\} = \{(\underline{\boldsymbol{\tau}}, 0) \in \underline{\mathbf{V}} : \text{div } \underline{\boldsymbol{\tau}} = 0, \text{ as}(\underline{\boldsymbol{\tau}}) = 0\}. \end{aligned} \quad (16)$$

identify precisely those variables that remain uncoupled by \mathcal{B} and therefore govern the stability of the saddle-point problem (14). On the kernel spaces the energy forms decouple: on K the form \mathcal{A} sees only the symmetric, divergence-free stress and is therefore coercive, whereas on H the Darcy energy $\mathcal{A}_{\mathbf{w}}$ sees only the divergence-free velocity and is coercive there. It remains to establish the inf-sup stability of \mathcal{B} on the orthogonal complement

$$H^\perp = \left\{ (\mathbf{w}, \mathbf{u}, \boldsymbol{\xi}) \in \mathbf{Q} : (\mathbf{w}, \mathbf{z})_0 = 0 \ \forall \mathbf{z} \in \mathbf{H}(\text{div}, \Omega), \text{ div } \mathbf{z} = 0 \right\}.$$

Since the divergence operator on $\mathbf{H}(\text{div}, \Omega)$ has closed range on bounded Lipschitz domains, its restriction to the L^2 -orthogonal complement of the divergence-free subspace is injective with bounded inverse. Consequently, on H^\perp the velocity component satisfies

$$\|\mathbf{w}\|_{H(\text{div})} \lesssim \|\text{div } \mathbf{w}\|_0.$$

Together with the trivial inequality $\|\text{div } \mathbf{w}\|_0 \leq \|\mathbf{w}\|_{H(\text{div})}$, this yields the norm equivalence

$$\|\mathbf{w}\|_{H(\text{div})} \simeq \|\text{div } \mathbf{w}\|_0 \quad \text{on } H^\perp.$$

Let $\mathbf{q} = (\mathbf{w}, \mathbf{u}, \boldsymbol{\xi}) \in H^\perp$. Choose $q_* = \text{div } \mathbf{w}$ and select $\underline{\boldsymbol{\tau}}_* \in \mathbf{H}(\text{div}, \Omega)$ according to (10) such that $\text{div } \underline{\boldsymbol{\tau}}_* = \mathbf{u}$. Then

$$\mathcal{B}((\underline{\boldsymbol{\tau}}_*, q_*), \mathbf{q}) = (q_*, \text{div } \mathbf{w}) + (\mathbf{u}, \text{div } \underline{\boldsymbol{\tau}}_*) + (\boldsymbol{\xi} \cdot \boldsymbol{\chi}, \underline{\boldsymbol{\tau}}_*) \gtrsim \|\text{div } \mathbf{w}\|_0^2 + \|\mathbf{u}\|_0^2 + \|\boldsymbol{\xi}\|_0^2.$$

Moreover,

$$\|(\underline{\boldsymbol{\tau}}_*, q_*)\|_{\underline{\mathbf{V}}} \lesssim \|\mathbf{u}\|_0 + \|\boldsymbol{\xi}\|_0 + \|\text{div } \mathbf{w}\|_0.$$

Using the norm equivalence on H^\perp , we conclude that

$$\inf_{0 \neq \mathbf{q} \in H^\perp} \sup_{0 \neq \underline{\mathbf{v}} \in \underline{\mathbf{V}}} \frac{\mathcal{B}(\underline{\mathbf{v}}, \mathbf{q})}{\|\underline{\mathbf{v}}\|_{\underline{\mathbf{V}}} \|\mathbf{q}\|_{\mathbf{Q}}} \geq \beta$$

for some constant $\beta > 0$ independent of the data. We are therefore in the setting of a perturbed saddle-point problem with coercivity of \mathcal{A} on K , coercivity of $\mathcal{A}_{\mathbf{w}}$ on H , and inf-sup stability of \mathcal{B} on H^\perp . This yields the following well-posedness result.

Theorem 1. *Let Ω be a bounded, connected Lipschitz domain. Assume that the Lamé parameters μ, λ , the storage coefficient \tilde{c}_0 , and the Biot parameter $\tilde{\alpha}$ are strictly positive, and that the permeability tensor $\boldsymbol{\kappa}$ is symmetric and uniformly elliptic. Given $\tilde{\mathbf{f}} \in L^2(\Omega)$ and $\mathbf{g} \in L^2(\Omega)^d$, the saddle-point problem (14) admits a unique solution $(\underline{\mathbf{u}}, \mathbf{p}) \in \underline{\mathbf{V}} \times \mathbf{Q}$. Moreover, there exists a constant $C > 0$ such that the stability estimate*

$$\|\underline{\mathbf{u}}\|_{\underline{\mathbf{V}}} + \|\mathbf{p}\|_{\mathbf{Q}} \leq C \left(\|\mathcal{F}\|_{\underline{\mathbf{V}'}} + \|\mathcal{G}\|_{\mathbf{Q}'} \right)$$

holds.

4 Finite element formulation

We now consider a shape-regular finite element triangulation \mathcal{T} of Ω . The mesh induces the set of element faces (or edges in $d = 2$) \mathcal{E} , which is assumed to respect the boundary decomposition. For each element $T \in \mathcal{T}$ we denote by $h_T := \text{diam}(T)$ its diameter, and define the global mesh size by

$$h := \max_{T \in \mathcal{T}} h_T.$$

A conforming Galerkin discretization of order $k \geq 0$ of the mixed formulation (14) consists in selecting finite element subspaces

$$\underline{\mathbf{V}}_{\mathcal{T}} \subset \underline{\mathbf{V}}, \quad \underline{\mathbf{Q}}_{\mathcal{T}} \subset \underline{\mathbf{Q}},$$

constructed from polynomial spaces

$$P_k(\mathcal{T}) = \{u \in L^2(\Omega) : u|_T \in \mathbb{P}_k(T) \forall T \in \mathcal{T}\}, \quad \mathbf{P}_k(\mathcal{T}) = P_k(\mathcal{T})^d,$$

where $\mathbb{P}_k(T)$ denotes the space of scalar polynomials of total degree at most k on the element T . Altogether, by employing the Galerkin method to (13), the fully-discrete solution for a single time step reads: for given data $\underline{\boldsymbol{\sigma}}^{n-1} \in \underline{\boldsymbol{\Sigma}}_{\mathcal{T}}$ and $p^{n-1} \in P_{\mathcal{T}}$ at the previous time step, seek $(\underline{\boldsymbol{\sigma}}, p, \mathbf{w}, \mathbf{u}, \boldsymbol{\xi}) \in \underline{\mathbf{X}}_{\mathcal{T}} = \underline{\mathbf{V}}_{\mathcal{T}} \times \underline{\mathbf{Q}}_{\mathcal{T}} \subset \underline{\mathbf{X}}$ such that for all $(\underline{\boldsymbol{\tau}}, q, \mathbf{z}, \mathbf{v}, \boldsymbol{\eta}) \in \underline{\mathbf{X}}_{\mathcal{T}}$ it holds

$$\begin{aligned} \mathcal{A}_{\underline{\boldsymbol{\sigma}}}(\underline{\boldsymbol{\sigma}}, \underline{\boldsymbol{\tau}}) + \tilde{\alpha}(p, \text{tr}(\underline{\boldsymbol{\tau}})) + (\mathbf{u}, \text{div} \underline{\boldsymbol{\tau}}) + (\boldsymbol{\xi} \cdot \boldsymbol{\chi}, \underline{\boldsymbol{\tau}}) &= 0 \\ \tilde{\alpha}(\text{tr} \underline{\boldsymbol{\sigma}}, q) + \mathcal{A}_p(p, q) + (\text{div} \mathbf{w}, q) &= \Delta t(f, q) + \tilde{\alpha}(\text{tr} \underline{\boldsymbol{\sigma}}^{n-1}, q) + \mathcal{A}_p(p^{n-1}, q) \\ (\text{div} \underline{\boldsymbol{\sigma}}, \mathbf{v}) &= -(\mathbf{g}, \mathbf{v}) \\ (\underline{\boldsymbol{\sigma}}, \boldsymbol{\eta} \cdot \boldsymbol{\chi}) &= 0 \\ (p, \text{div} \mathbf{z}) - \frac{1}{\Delta t} \mathcal{A}_{\mathbf{w}}(\mathbf{w}, \mathbf{z}) &= 0. \end{aligned} \tag{18}$$

In compact notation, as introduced in section 3, the discrete solutions $\underline{\mathbf{u}}_{\mathcal{T}} \in \underline{\mathbf{V}}_{\mathcal{T}} = \underline{\boldsymbol{\Sigma}}_{\mathcal{T}} \times P_{\mathcal{T}}$ and $\mathbf{p}_{\mathcal{T}} \in \underline{\mathbf{Q}}_{\mathcal{T}} = \mathbf{W}_{\mathcal{T}} \times \mathbf{U}_{\mathcal{T}} \times \boldsymbol{\Xi}_{\mathcal{T}}$ satisfy

$$\begin{aligned} \mathcal{A}(\underline{\mathbf{u}}_{\mathcal{T}}, \underline{\mathbf{v}}) + \mathcal{B}(\underline{\mathbf{v}}, \mathbf{p}_{\mathcal{T}}) &= \mathcal{F}(\underline{\mathbf{v}}) \\ \mathcal{B}(\underline{\mathbf{u}}_{\mathcal{T}}, \mathbf{q}) - \mathcal{C}(\mathbf{p}_{\mathcal{T}}, \mathbf{q}) &= \mathcal{G}(\mathbf{q}) \end{aligned} \tag{19}$$

for all $(\underline{\mathbf{v}}, \mathbf{q}) \in \underline{\mathbf{V}}_{\mathcal{T}} \times \underline{\mathbf{Q}}_{\mathcal{T}}$.

The bilinear form \mathcal{B} induces the discrete kernel spaces

$$H_{\mathcal{T}} = \{\mathbf{q} \in \underline{\mathbf{Q}}_{\mathcal{T}} : \mathcal{B}(\underline{\mathbf{v}}, \mathbf{q}) = 0 \forall \underline{\mathbf{v}} \in \underline{\mathbf{V}}_{\mathcal{T}}\}, \tag{20}$$

$$K_{\mathcal{T}} = \{\underline{\mathbf{v}} \in \underline{\mathbf{V}}_{\mathcal{T}} : \mathcal{B}(\underline{\mathbf{v}}, \mathbf{q}) = 0 \forall \mathbf{q} \in \underline{\mathbf{Q}}_{\mathcal{T}}\}. \tag{21}$$

In order to mimic the structural properties of the continuous formulation, we assume that the discrete spaces are chosen such that the kernel structure of the bilinear form \mathcal{B} is preserved at the discrete level.

Lemma 1. *Assume the discrete spaces satisfy $\text{div}(\mathbf{W}_{\mathcal{T}}) \subseteq P_{\mathcal{T}}$ as well as*

(A) *There exists $\beta_u > 0$, independent of the mesh-size, such that*

$$\inf_{0 \neq \mathbf{u} \in \mathbf{U}_{\mathcal{T}}} \sup_{0 \neq \underline{\boldsymbol{\tau}} \in \underline{\boldsymbol{\Sigma}}_{\mathcal{T}}} \frac{(\mathbf{u}, \text{div} \underline{\boldsymbol{\tau}})}{\|\underline{\boldsymbol{\tau}}\|_{H(\text{div})} \|\mathbf{u}\|_0} \geq \beta_u. \tag{22}$$

(B) *There exists a finite-dimensional space $\boldsymbol{\Psi}_{\mathcal{T}} \subset H_0^1(\Omega)^d$ such that*

$$\text{curl} \boldsymbol{\Psi}_{\mathcal{T}} \subseteq \underline{\boldsymbol{\Sigma}}_{\mathcal{T}},$$

and there exists $\beta_{\xi} > 0$, independent of h , such that

$$\inf_{0 \neq \boldsymbol{\xi} \in \boldsymbol{\Xi}_{\mathcal{T}}} \sup_{0 \neq \psi \in \boldsymbol{\Psi}_{\mathcal{T}}} \frac{(\text{div} \psi, \boldsymbol{\xi})}{\|\psi\|_1 \|\boldsymbol{\xi}\|_0} \geq \beta_{\xi}. \tag{23}$$

Then:

$$H_{\mathcal{T}} = \{(\mathbf{w}, 0, 0) \in \mathbf{Q}_{\mathcal{T}} : (q, \operatorname{div} \mathbf{w}) = 0 \ \forall q \in P_{\mathcal{T}}\}, \quad (24a)$$

$$K_{\mathcal{T}} = \left\{(\underline{\boldsymbol{\tau}}, q) \in \underline{\mathbf{V}}_{\mathcal{T}} : (q, \operatorname{div} \mathbf{w}) = 0 \ \forall \mathbf{w} \in \mathbf{W}_{\mathcal{T}}, (\mathbf{u}, \operatorname{div} \underline{\boldsymbol{\tau}}) = 0 \ \forall \mathbf{u} \in \mathbf{U}_{\mathcal{T}}, (\boldsymbol{\eta} \cdot \boldsymbol{\chi}, \underline{\boldsymbol{\tau}}) = 0 \ \forall \boldsymbol{\eta} \in \boldsymbol{\Xi}_{\mathcal{T}}\right\}. \quad (24b)$$

Proof. Let $\mathbf{q} = (\mathbf{w}, \mathbf{u}, \boldsymbol{\xi}) \in H_{\mathcal{T}}$. By definition, $\mathcal{B}(\underline{\mathbf{v}}, \mathbf{q}) = 0 \quad \forall \underline{\mathbf{v}} = (\underline{\boldsymbol{\tau}}, q) \in \underline{\mathbf{V}}_{\mathcal{T}}$. Choosing $\underline{\mathbf{v}} = (0, q)$ with arbitrary $q \in P_{\mathcal{T}}$ yields

$$0 = \mathcal{B}((0, q), (\mathbf{w}, \mathbf{u}, \boldsymbol{\xi})) = (q, \operatorname{div} \mathbf{w}) \quad \forall q \in P_{\mathcal{T}}. \quad (25)$$

Since $\operatorname{div} \mathbf{w} \in \operatorname{div}(\mathbf{W}_{\mathcal{T}}) \subseteq P_{\mathcal{T}}$, we may take $q = \operatorname{div} \mathbf{w}$ in (25) and obtain

$$\|\operatorname{div} \mathbf{w}\|_0^2 = (\operatorname{div} \mathbf{w}, \operatorname{div} \mathbf{w}) = 0,$$

hence $\operatorname{div} \mathbf{w} = 0$. Next choose $\underline{\mathbf{v}} = (\underline{\boldsymbol{\tau}}, 0)$ with arbitrary $\underline{\boldsymbol{\tau}} \in \underline{\boldsymbol{\Sigma}}_{\mathcal{T}}$. Then

$$0 = \mathcal{B}((\underline{\boldsymbol{\tau}}, 0), (\mathbf{w}, \mathbf{u}, \boldsymbol{\xi})) = (\mathbf{u}, \operatorname{div} \underline{\boldsymbol{\tau}}) + (\boldsymbol{\xi} \cdot \boldsymbol{\chi}, \underline{\boldsymbol{\tau}}) \quad \forall \underline{\boldsymbol{\tau}} \in \underline{\boldsymbol{\Sigma}}_{\mathcal{T}}. \quad (26)$$

Pick $\underline{\boldsymbol{\tau}} = \operatorname{curl} \psi$ with $\psi \in \boldsymbol{\Psi}_{\mathcal{T}}$. Using $\operatorname{div}(\operatorname{curl} \psi) = 0$ (elementwise) gives

$$0 = (\mathbf{u}, \operatorname{div}(\operatorname{curl} \psi)) + (\boldsymbol{\xi} \cdot \boldsymbol{\chi}, \operatorname{curl} \psi) = (\operatorname{div} \psi, \boldsymbol{\xi}) \quad \forall \psi \in \boldsymbol{\Psi}_{\mathcal{T}}.$$

By the discrete inf-sup (23) we conclude $\boldsymbol{\xi} = 0$. With $\boldsymbol{\xi} = 0$, (26) reduces to

$$(\mathbf{u}, \operatorname{div} \underline{\boldsymbol{\tau}}) = 0 \quad \forall \underline{\boldsymbol{\tau}} \in \underline{\boldsymbol{\Sigma}}_{\mathcal{T}},$$

and (22) implies $\mathbf{u} = 0$. Thus $\mathbf{q} = (\mathbf{w}, 0, 0)$ and $\operatorname{div} \mathbf{w} = 0$, i.e. $H_{\mathcal{T}} \subseteq \{(\mathbf{w}, 0, 0) : \operatorname{div} \mathbf{w} = 0\}$.

Conversely, if $\mathbf{q} = (\mathbf{w}, 0, 0)$ with $\operatorname{div} \mathbf{w} = 0$, then for any $\underline{\mathbf{v}} = (\underline{\boldsymbol{\tau}}, q) \in \underline{\mathbf{V}}_{\mathcal{T}}$,

$$\mathcal{B}(\underline{\mathbf{v}}, \mathbf{q}) = (q, \operatorname{div} \mathbf{w}) = 0,$$

hence $\mathbf{q} \in H_{\mathcal{T}}$ and (24a) follows.

Now, let $\underline{\mathbf{v}} = (\underline{\boldsymbol{\tau}}, q) \in K_{\mathcal{T}}$. By definition, $\mathcal{B}(\underline{\mathbf{v}}, \mathbf{q}) = 0 \quad \forall \mathbf{q} = (\mathbf{w}, \mathbf{u}, \boldsymbol{\xi}) \in \mathbf{Q}_{\mathcal{T}}$. Testing with $\mathbf{q} = (\mathbf{w}, 0, 0)$ for arbitrary $\mathbf{w} \in \mathbf{W}_{\mathcal{T}}$ gives

$$0 = \mathcal{B}((\underline{\boldsymbol{\tau}}, q), (\mathbf{w}, 0, 0)) = (q, \operatorname{div} \mathbf{w}) \quad \forall \mathbf{w} \in \mathbf{W}_{\mathcal{T}},$$

i.e. $(q, \operatorname{div} \mathbf{w}) = 0$ for all $\mathbf{w} \in \mathbf{W}_{\mathcal{T}}$. Testing with $\mathbf{q} = (0, \mathbf{u}, 0)$ for arbitrary $\mathbf{u} \in \mathbf{U}_{\mathcal{T}}$ yields

$$0 = \mathcal{B}((\underline{\boldsymbol{\tau}}, q), (0, \mathbf{u}, 0)) = (\mathbf{u}, \operatorname{div} \underline{\boldsymbol{\tau}}) \quad \forall \mathbf{u} \in \mathbf{U}_{\mathcal{T}}.$$

Testing with $\mathbf{q} = (0, 0, \boldsymbol{\eta})$ for arbitrary $\boldsymbol{\eta} \in \boldsymbol{\Xi}_{\mathcal{T}}$ gives

$$0 = \mathcal{B}((\underline{\boldsymbol{\tau}}, q), (0, 0, \boldsymbol{\eta})) = (\boldsymbol{\eta} \cdot \boldsymbol{\chi}, \underline{\boldsymbol{\tau}}) \quad \forall \boldsymbol{\eta} \in \boldsymbol{\Xi}_{\mathcal{T}}$$

and every $(\underline{\boldsymbol{\tau}}, q) \in K_{\mathcal{T}}$ satisfies the three orthogonality conditions in (24b). Conversely, let $(\underline{\boldsymbol{\tau}}, q) \in \underline{\mathbf{V}}_{\mathcal{T}}$ satisfy

$$(q, \operatorname{div} \mathbf{w}) = 0 \quad \forall \mathbf{w} \in \mathbf{W}_{\mathcal{T}}, \quad (\mathbf{u}, \operatorname{div} \underline{\boldsymbol{\tau}}) = 0 \quad \forall \mathbf{u} \in \mathbf{U}_{\mathcal{T}} \quad \text{and} \quad (\boldsymbol{\eta} \cdot \boldsymbol{\chi}, \underline{\boldsymbol{\tau}}) = 0 \quad \forall \boldsymbol{\eta} \in \boldsymbol{\Xi}_{\mathcal{T}}.$$

Then for every $\mathbf{q} = (\mathbf{w}, \mathbf{u}, \boldsymbol{\xi}) \in \mathbf{Q}_{\mathcal{T}}$,

$$\mathcal{B}((\underline{\boldsymbol{\tau}}, q), \mathbf{q}) = (q, \operatorname{div} \mathbf{w}) + (\mathbf{u}, \operatorname{div} \underline{\boldsymbol{\tau}}) + (\boldsymbol{\xi} \cdot \boldsymbol{\chi}, \underline{\boldsymbol{\tau}}) = 0.$$

Thus $(\underline{\boldsymbol{\tau}}, q) \in K_{\mathcal{T}}$, and (24b) follows. □

Remark 1. *If, in addition, $\operatorname{div}(\mathbf{W}_{\mathcal{T}}) = P_{\mathcal{T}}$, then the first orthogonality condition in (24b) implies $q = 0$, and therefore*

$$K_{\mathcal{T}} = \left\{(\underline{\boldsymbol{\tau}}, 0) \in \underline{\mathbf{V}}_{\mathcal{T}} : (\mathbf{u}, \operatorname{div} \underline{\boldsymbol{\tau}}) = 0 \ \forall \mathbf{u} \in \mathbf{U}_{\mathcal{T}}, \quad (\boldsymbol{\eta} \cdot \boldsymbol{\chi}, \underline{\boldsymbol{\tau}}) = 0 \ \forall \boldsymbol{\eta} \in \boldsymbol{\Xi}_{\mathcal{T}}\right\}.$$

By Lemma 1, the discrete kernels $H_{\mathcal{T}}$ and $K_{\mathcal{T}}$ satisfy the same structural constraints as their continuous counterparts. On $H_{\mathcal{T}}$, any element has the form $(\mathbf{w}, 0, 0)$ with $\operatorname{div} \mathbf{w} = 0$. Hence, by uniform ellipticity of κ^{-1} ,

$$\mathcal{A}_{\bar{\mathbf{w}}}(\mathbf{w}, \mathbf{w}) = (\kappa^{-1} \mathbf{w}, \mathbf{w}) \geq \alpha_w \|\mathbf{w}\|_{H(\operatorname{div})}^2 \quad \forall (\mathbf{w}, 0, 0) \in H_{\mathcal{T}}.$$

On $K_{\mathcal{T}}$, the divergence-free condition and the discrete weak symmetry constraint eliminate the nullspace of the compliance operator. Therefore, the uniform positivity of \mathcal{A} implies that there exists $\alpha_\sigma > 0$ such that

$$\mathcal{A}((\underline{\boldsymbol{\tau}}, q), (\underline{\boldsymbol{\tau}}, q)) \geq \alpha_\sigma (\|\underline{\boldsymbol{\tau}}\|_{H(\operatorname{div})}^2 + \|q\|_0^2) \quad \forall (\underline{\boldsymbol{\tau}}, q) \in K_{\mathcal{T}}.$$

With coercivity established, the well-posedness of the discrete problem (19) now depends solely on the satisfaction of the discrete inf-sup condition for the bilinear form \mathcal{B} , which we analyze in the following lemma.

Lemma 2. *Assume that $\operatorname{div}(\mathbf{W}_{\mathcal{T}}) \subseteq P_{\mathcal{T}}$ and that the discrete elasticity stability conditions (A)–(B) of Lemma 1 hold. Then there exists $\beta_{\mathcal{T}} > 0$, independent of the mesh-size, such that*

$$\inf_{0 \neq \mathbf{q} \in H_{\mathcal{T}}^\perp} \sup_{0 \neq \mathbf{v} \in \mathbf{V}_{\mathcal{T}}} \frac{\mathcal{B}(\mathbf{v}, \mathbf{q})}{\|\mathbf{v}\|_{\mathbf{V}} \|\mathbf{q}\|_{\mathbf{Q}}} \geq \beta_{\mathcal{T}} \quad (27)$$

and the discrete problem (19) admits a unique solution $(\underline{\mathbf{u}}_{\mathcal{T}}, \mathbf{p}_{\mathcal{T}}) \in \mathbf{V}_{\mathcal{T}} \times \mathbf{Q}_{\mathcal{T}}$. Moreover, the stability estimate

$$\|\underline{\mathbf{u}}_{\mathcal{T}}\|_{\mathbf{V}} + \|\mathbf{p}_{\mathcal{T}}\|_{\mathbf{Q}} \leq C \left(\|\mathcal{F}\|_{\mathbf{V}'} + \|\mathcal{G}\|_{\mathbf{Q}'} \right)$$

holds with a constant $C > 0$ independent of the mesh-size.

Proof. Let $\mathbf{q} = (\mathbf{w}, \mathbf{u}, \boldsymbol{\xi}) \in H_{\mathcal{T}}^\perp$ be arbitrary. By definition of $H_{\mathcal{T}}^\perp$, the velocity component $\mathbf{w} \in \mathbf{W}_{\mathcal{T}}$ satisfies the orthogonality condition defining $H_{\mathcal{T}}^\perp$. Hence

$$\|\mathbf{w}\|_{H(\operatorname{div})} \approx \|\operatorname{div} \mathbf{w}\|_0 \quad \text{for } \mathbf{w} \in H_{\mathcal{T}}^\perp. \quad (28)$$

Choose

$$q_* := \operatorname{div} \mathbf{w} \in P_{\mathcal{T}},$$

which is admissible since $\operatorname{div}(\mathbf{W}_{\mathcal{T}}) \subseteq P_{\mathcal{T}}$. Next, apply the assumptions (A) and (B) from Lemma 1 to obtain a stress test function $\underline{\boldsymbol{\tau}}_* \in \underline{\boldsymbol{\Sigma}}_{\mathcal{T}}$ such that

$$(\mathbf{u}, \operatorname{div} \underline{\boldsymbol{\tau}}_*) + (\boldsymbol{\xi} \cdot \boldsymbol{\chi}, \underline{\boldsymbol{\tau}}_*) \gtrsim \|\mathbf{u}\|_0^2 + \|\boldsymbol{\xi}\|_0^2, \quad \|\underline{\boldsymbol{\tau}}_*\|_{H(\operatorname{div})} \lesssim \|\mathbf{u}\|_0 + \|\boldsymbol{\xi}\|_0. \quad (29)$$

Define $\underline{\mathbf{v}}_* := (\underline{\boldsymbol{\tau}}_*, q_*) \in \mathbf{V}_{\mathcal{T}}$. Then, by definition of \mathcal{B} ,

$$\mathcal{B}(\underline{\mathbf{v}}_*, \mathbf{q}) = (q_*, \operatorname{div} \mathbf{w}) + (\mathbf{u}, \operatorname{div} \underline{\boldsymbol{\tau}}_*) + (\boldsymbol{\xi} \cdot \boldsymbol{\chi}, \underline{\boldsymbol{\tau}}_*).$$

Using $q_* = \operatorname{div} \mathbf{w}$ and (29),

$$\mathcal{B}(\underline{\mathbf{v}}_*, \mathbf{q}) \gtrsim \|\operatorname{div} \mathbf{w}\|_0^2 + \|\mathbf{u}\|_0^2 + \|\boldsymbol{\xi}\|_0^2. \quad (30)$$

Moreover,

$$\|\underline{\mathbf{v}}_*\|_{\mathbf{V}} \lesssim \|\underline{\boldsymbol{\tau}}_*\|_{H(\operatorname{div})} + \|q_*\|_0 \lesssim \|\mathbf{u}\|_0 + \|\boldsymbol{\xi}\|_0 + \|\operatorname{div} \mathbf{w}\|_0.$$

Combining with (28) gives

$$\|\mathbf{q}\|_{\mathbf{Q}} = \left(\|\mathbf{w}\|_{H(\operatorname{div})}^2 + \|\mathbf{u}\|_0^2 + \|\boldsymbol{\xi}\|_0^2 \right)^{1/2} \approx \left(\|\operatorname{div} \mathbf{w}\|_0^2 + \|\mathbf{u}\|_0^2 + \|\boldsymbol{\xi}\|_0^2 \right)^{1/2}.$$

Therefore, (30) implies

$$\frac{\mathcal{B}(\underline{\mathbf{v}}_*, \mathbf{q})}{\|\underline{\mathbf{v}}_*\|_{\mathbf{V}} \|\mathbf{q}\|_{\mathbf{Q}}} \gtrsim 1,$$

with constants independent of the mesh-size. Taking the supremum over $\mathbf{v} \in \mathbf{V}_{\mathcal{T}}$ and then the infimum over $\mathbf{q} \in H_{\mathcal{T}}^\perp \setminus \{0\}$ yields (27). \square

We now list standard finite element families that satisfy assumptions (A)–(B) of Lemma 1 as well as the Darcy compatibility condition $\operatorname{div}(\mathbf{W}_{\mathcal{T}}) \subseteq P_{\mathcal{T}}$. We distinguish between simplicial and tensor-product meshes.

4.1 Finite elements on simplicial meshes

We start with $H(\text{div})$ -conforming finite element spaces on simplices and define the global velocity and stress spaces by

$$\mathbf{W}_{\mathcal{T}} := \{\mathbf{z} \in \mathbf{H}(\text{div}, \Omega) : \mathbf{z}|_T \in \mathbf{Y}_{\ell}(T) \forall T \in \mathcal{T}\}, \text{ and } \underline{\Sigma}_{\mathcal{T}} := \{\underline{\boldsymbol{\tau}} \in \mathbf{H}(\text{div}, \Omega) : (\underline{\boldsymbol{\tau}}_i)|_T \in \mathbf{X}_k(T) \forall T \in \mathcal{T}, i = 1, \dots, d\},$$

where the local spaces $\mathbf{X}_k(T)$ and $\mathbf{Y}_{\ell}(T)$ are chosen from the classical families

$$\mathbf{X}_k(T), \mathbf{Y}_{\ell}(T) \in \{\mathbf{RT}_k(T), \mathbf{BDM}_k(T), \mathbf{BDFM}_k(T), \mathbf{ABF}_k(T)\},$$

with

$$\begin{aligned} \mathbf{RT}_k(T) &:= \mathbb{P}_k(T)^d + \mathbf{x} \mathbb{P}_k(T), \\ \mathbf{BDM}_k(T) &:= \mathbb{P}_k(T)^d, \quad k \geq 1, \\ \mathbf{ABF}_k(T) &:= \mathbb{P}_k(T)^d + \mathbf{x} \mathbb{P}_k(T)^d, \quad k \geq 1, \\ \mathbf{BDFM}_k(T) &:= \mathbf{RT}_k(T) \oplus (b_T \mathbb{P}_{k-1}(T)^d), \quad k \geq 1. \end{aligned}$$

Here \mathbf{x} denotes the identity map on T , and

$$b_T = \prod_{i=1}^{d+1} \lambda_i$$

is the element bubble function defined in terms of the barycentric coordinates λ_i of T .

The scalar spaces $\mathbf{U}_{\mathcal{T}}$ and $P_{\mathcal{T}}$ are then chosen according to the divergence constraints appearing in Lemma 1. More precisely, the displacement space $\mathbf{U}_{\mathcal{T}}$ is selected so that assumption **(A)** holds, while the pressure space $P_{\mathcal{T}}$ is chosen such that

$$\text{div}(\mathbf{W}_{\mathcal{T}}) \subseteq P_{\mathcal{T}}.$$

For the classical $H(\text{div})$ -conforming families introduced above, the divergence operator is surjective onto the corresponding polynomial spaces, i.e.,

$$\text{div } \mathbf{RT}_k(T) = \mathbb{P}_k(T), \quad \text{div } \mathbf{BDM}_k(T) = \text{div } \mathbf{BDFM}_k(T) = \text{div } \mathbf{ABF}_k(T) = \mathbb{P}_{k-1}(T).$$

Hence the minimal compatible choices for $\mathbf{U}_{\mathcal{T}}$ and $P_{\mathcal{T}}$ coincide with the discontinuous polynomial spaces

$$\mathbf{U}_{\mathcal{T}} = \mathbb{P}_k(\mathcal{T})^d \quad \text{if } \underline{\Sigma}_{\mathcal{T}} \text{ is based on } \mathbf{RT}_k, \quad \mathbf{U}_{\mathcal{T}} = \mathbb{P}_{k-1}(\mathcal{T})^d \quad \text{if } \underline{\Sigma}_{\mathcal{T}} \text{ is based on } \mathbf{BDM}_k, \mathbf{BDFM}_k, \text{ or } \mathbf{ABF}_k,$$

and similarly

$$P_{\mathcal{T}} = \mathbb{P}_{\ell}(\mathcal{T}) \quad \text{if } \mathbf{W}_{\mathcal{T}} \text{ is based on } \mathbf{RT}_{\ell}, \quad P_{\mathcal{T}} = \mathbb{P}_{\ell-1}(\mathcal{T}) \quad \text{if } \mathbf{W}_{\mathcal{T}} \text{ is based on } \mathbf{BDM}_{\ell}, \mathbf{BDFM}_{\ell}, \text{ or } \mathbf{ABF}_{\ell}.$$

It remains to choose the spaces $\Psi_{\mathcal{T}}$ and $\Xi_{\mathcal{T}}$ appearing in assumption **(B)**. To this end we consider the Stokes-stable pairs

$$\Psi_{\mathcal{T}} := \{\psi \in H_0^1(\Omega)^d : \psi|_T \in \Psi_r(T) \forall T \in \mathcal{T}\}, \quad \Xi_{\mathcal{T}} := \{\boldsymbol{\xi} \in L^2(\Omega)^{2d-3} : \boldsymbol{\xi}|_T \in \Xi_r(T) \forall T \in \mathcal{T}\}$$

with the following possibilities.

- Taylor–Hood elements $(\Psi_r(T), \Xi_r(T)) = (\mathbb{P}_{r+1}(T)^d, \mathbb{P}_r(T)^{2d-3})$ for $r \geq 1$. Since $\text{curl } \Psi_r(\mathcal{T}) \subseteq \mathbb{P}_r(\mathcal{T})^d$, the inclusion $\text{curl } \Psi_{\mathcal{T}} \subseteq \underline{\Sigma}_{\mathcal{T}}$ holds provided that $r \leq k$. Here, the **BDM** case coincides with the Arnold–Falk–Winther choice.
- Mini elements $(\Psi(T), \Xi(T)) = (\mathbb{P}_1(T)^d \oplus B_{d+1}(T)^d, \mathbb{P}_1(T)^{2d-3})$, where $B_{d+1}(T)$ denotes the element bubble of degree $d+1$. Since $\text{curl } \Psi(\mathcal{T}) \subseteq \mathbb{P}_d(\mathcal{T})^d$, the inclusion $\text{curl } \Psi_{\mathcal{T}} \subseteq \underline{\Sigma}_{\mathcal{T}}$ holds provided that $d \leq k$.
- Scott–Vogelius elements $(\Psi_r(T), \Xi_r(T)) = (\mathbb{P}_r(T)^d, \mathbb{P}_{r-1}(T)^{2d-3})$, for $r \geq 2d$ under additional mesh conditions. Since $\text{curl } \Psi_r(\mathcal{T}) \subseteq \mathbb{P}_{r-1}(\mathcal{T})^d$, the inclusion $\text{curl } \Psi_{\mathcal{T}} \subseteq \underline{\Sigma}_{\mathcal{T}}$ holds provided that $r \leq k+1$.

4.2 Finite elements on tensor-product meshes

We now consider tensor-product meshes and let \mathcal{T} be a shape-regular partition of Ω into quadrilaterals for $d = 2$ or hexahedra for $d = 3$. On such meshes, let $\mathcal{Q}_{\mathbf{r}}(T)$ denote the tensor-product polynomial space on T with multi-degree $\mathbf{r} = (r_1, \dots, r_d)$, i.e.

$$\mathcal{Q}_{\mathbf{r}}(T) := \text{span}\{x_1^{\alpha_1} \cdots x_d^{\alpha_d} : 0 \leq \alpha_i \leq r_i, i = 1, \dots, d\}.$$

In particular, we write $\mathcal{Q}_k(T) := \mathcal{Q}_{(k, \dots, k)}(T)$. As before, we define the global velocity and stress spaces by

$$\mathbf{W}_{\mathcal{T}} := \{\mathbf{z} \in \mathbf{H}(\text{div}, \Omega) : \mathbf{z}|_T \in \mathbf{Y}_{\ell}(T) \forall T \in \mathcal{T}\}, \quad \underline{\Sigma}_{\mathcal{T}} := \{\underline{\boldsymbol{\tau}} \in \mathbf{H}(\text{div}, \Omega) : (\underline{\boldsymbol{\tau}}_i)|_T \in \mathbf{X}_k(T) \forall T \in \mathcal{T}, i = 1, \dots, d\}.$$

The local spaces $\mathbf{X}_k(T)$ and $\mathbf{Y}_{\ell}(T)$ are chosen from the classical tensor-product $H(\text{div})$ families

$$\mathbf{X}_k(T), \mathbf{Y}_{\ell}(T) \in \{\mathbf{RT}_k(T), \mathbf{BDDF}_k(T)\}.$$

with

$$\mathbf{RT}_k(T) = \begin{cases} \mathcal{Q}_{k+1,k}(T) \times \mathcal{Q}_{k,k+1}(T) & d = 2 \\ \mathcal{Q}_{k+1,k,k}(T) \times \mathcal{Q}_{k,k+1,k}(T) \times \mathcal{Q}_{k,k,k+1}(T) & d = 3 \end{cases} \text{ and } \mathbf{BDDF}_k(T) := \mathcal{Q}_k(T)^d, \quad k \geq 1.$$

For the classical tensor-product $H(\text{div})$ -conforming families introduced above, the divergence operator maps onto the corresponding scalar polynomial spaces, i.e. $\text{div } \mathbf{RT}_k(T) = \mathcal{Q}_k(T)$, and $\text{div } \mathbf{BDDF}_k(T) = \mathcal{Q}_{k-1}(T)$. Consequently, the minimal compatible scalar spaces are

$$\mathbf{U}_{\mathcal{T}} = \mathcal{Q}_k(\mathcal{T})^d \quad \text{if } \underline{\Sigma}_{\mathcal{T}} \text{ is based on } \mathbf{RT}_k, \quad \mathbf{U}_{\mathcal{T}} = \mathcal{Q}_{k-1}(\mathcal{T})^d \quad \text{if } \underline{\Sigma}_{\mathcal{T}} \text{ is based on } \mathbf{BDDF}_k,$$

and similarly

$$P_{\mathcal{T}} = \mathcal{Q}_{\ell}(\mathcal{T}) \quad \text{if } \mathbf{W}_{\mathcal{T}} \text{ is based on } \mathbf{RT}_{\ell}, \quad P_{\mathcal{T}} = \mathcal{Q}_{\ell-1}(\mathcal{T}) \quad \text{if } \mathbf{W}_{\mathcal{T}} \text{ is based on } \mathbf{BDDF}_{\ell}.$$

It remains to choose the spaces $\Psi_{\mathcal{T}}$ and $\Xi_{\mathcal{T}}$ appearing in assumption **(B)**. To this end we consider the Stokes-stable pairs

$$\Psi_{\mathcal{T}} := \{\psi \in H_0^1(\Omega)^d : \psi|_T \in \Psi_r(T) \forall T \in \mathcal{T}\}, \quad \Xi_{\mathcal{T}} := \{\boldsymbol{\xi} \in L^2(\Omega)^{2d-3} : \boldsymbol{\xi}|_T \in \Xi_r(T) \forall T \in \mathcal{T}\}.$$

A natural tensor-product analogue is given by the Taylor–Hood family

$$(\Psi_r(T), \Xi_r(T)) = (\mathcal{Q}_{r+1}(T)^d, \mathcal{Q}_r(T)^{2d-3}), \quad r \geq 1.$$

Since $\text{curl } \Psi_r(\mathcal{T}) \subseteq \mathcal{Q}_r(\mathcal{T})^d$, the inclusion $\text{curl } \Psi_{\mathcal{T}} \subseteq \underline{\Sigma}_{\mathcal{T}}$ holds provided that

$$r \leq k \quad \text{if } \mathbf{X}_k(T) = \mathbf{RT}_k(T), \quad r \leq k - 1 \quad \text{if } \mathbf{X}_k(T) = \mathbf{BDDF}_k(T).$$

Another possibility is the Mini element $(\Psi(T), \Xi(T)) = (\mathcal{Q}_1(T)^d \oplus B(T)^d, \mathcal{Q}_1(T)^{2d-3})$, where $B(T) = \prod_{i=1}^d (1 - x_i^2)$ denotes the tensor-product bubble function. Since $\text{curl } \Psi(\mathcal{T}) \subseteq \mathcal{Q}_1(\mathcal{T})^d$, the inclusion $\text{curl } \Psi_{\mathcal{T}} \subseteq \underline{\Sigma}_{\mathcal{T}}$ holds provided that

$$1 \leq k \quad \text{if } \mathbf{X}_k(T) = \mathbf{RT}_k(T), \quad 2 \leq k \quad \text{if } \mathbf{X}_k(T) = \mathbf{BDDF}_k(T).$$

5 Iterative coupling for the fully-discrete system

Our aim is to design an iterative coupling scheme for the fully-discrete formulation of the Biot equations (18), decoupling flow and mechanics solution; the scheme and discussion will be independent of the particular spatial discretization presented in Section 4. Due to the use of a stress-pressure based formulation, the coupling between the flow and mechanics subproblems is in fact symmetric; for a more detailed discussion on the inherent gradient flow structure and resulting symmetries, we refer to [14]. Symmetric couplings can be decoupled in iterative fashion by a simple alternating minimization approach, and its convergence follows from abstract results solely relying on convexity and continuity properties [13]. As discussed in [14] such a simple alternating minimization can be identified with the common fixed-stress split, cf., e.g., [22].

Inspired by previous problem-specific developments on tuned stabilization of the fixed-stress split, we investigate the possibility of using stabilization, introducing the possibility for tuning the convergence speed. However, due to the symmetric coupling, instead of adding stabilization, an improved approximation of the Schur complement is in fact provided by negative stabilization, i.e., seemingly destabilization, cf., e.g., [27]. A similar conclusion has been arrived in [11] for a different poromechanics model with symmetric coupling between displacements and fluxes.

Fixed-stress split Finally, resembling the same approach as the fixed-stress split, we consider a two-step iterative coupling scheme with $i \geq 1$ denoting the iteration index, which is performed until convergence in any user-defined norm. We introduce a destabilization parameter $\beta \geq 0$ (to be specified below based on convergence analysis), applied in a negative fashion. For simplicity, we assume initialization of the scheme through the use of the data at the previous time step. Then the following iteration i is repeated until convergence, defined by any user-defined stopping criterion.

Step 1: Flow Let $\underline{\sigma}^{i-1} \in \underline{\Sigma}_{\mathcal{T}}$ be given, seek $p^i, \mathbf{w}^i \in P_{\mathcal{T}} \times \mathbf{W}_{\mathcal{T}}$ such that for all $(q, \mathbf{z}) \in P_{\mathcal{T}} \times \mathbf{W}_{\mathcal{T}}$ it holds

$$\begin{aligned} \mathcal{A}_p(p^i, q) - \beta(p^i - p^{i-1}, q) &+ (\operatorname{div} \mathbf{w}^i, q) = \langle \tilde{f}, q \rangle - \tilde{\alpha}(\operatorname{tr} \underline{\sigma}^{i-1}, q) \\ (p^i, \operatorname{div} \mathbf{z}) &- \frac{1}{\Delta t} \mathcal{A}_{\tilde{\mathbf{w}}}(\mathbf{w}^i, \mathbf{z}) = 0. \end{aligned} \quad (31)$$

Step 2: Mechanics Seek $(\underline{\sigma}^i, \mathbf{u}^i, \boldsymbol{\xi}^i) \in \underline{\Sigma}_{\mathcal{T}} \times \mathbf{U}_{\mathcal{T}} \times \boldsymbol{\Xi}_{\mathcal{T}}$ such that for all $(\boldsymbol{\tau}, \mathbf{v}, \boldsymbol{\eta}) \in \underline{\Sigma}_{\mathcal{T}} \times \mathbf{U}_{\mathcal{T}} \times \boldsymbol{\Xi}_{\mathcal{T}}$ it holds

$$\begin{aligned} \mathcal{A}_{\underline{\sigma}}(\underline{\sigma}^i, \boldsymbol{\tau}) + (\mathbf{u}^i, \operatorname{div} \boldsymbol{\tau}) &+ (\boldsymbol{\xi}^i \cdot \boldsymbol{\chi}, \boldsymbol{\tau}) = -\tilde{\alpha}(p^i, \operatorname{tr}(\boldsymbol{\tau})) \\ (\operatorname{div} \underline{\sigma}^i, \mathbf{v}) &= -(\mathbf{g}, \mathbf{v}) \\ (\underline{\sigma}^i, \boldsymbol{\eta} \cdot \boldsymbol{\chi}) &= 0. \end{aligned} \quad (32)$$

Remark 2 (Standard fixed-stress split). *The choice $\beta = 0$ resembles the standard fixed-stress split, iterating between solving the flow problem under fixed stress conditions, and updating the mechanics variables subsequently. It is unconditionally convergent for the symmetric problem [14, 13].*

We employ a problem-specific analysis to identify suitable values for $\beta \geq 0$ with optimized convergence rate in terms of the fluid pressure, following mostly the techniques in [15].

Lemma 3 (Convergence of a tuned fixed-stress split). *Let $i \geq 1$ and $(\underline{\sigma}, p, \mathbf{w}, \mathbf{u}, \boldsymbol{\xi}) \in \mathbf{X}_{\mathcal{T}}$ and $(\underline{\sigma}^i, p^i, \mathbf{w}^i, \mathbf{u}^i, \boldsymbol{\xi}^i) \in \mathbf{X}_{\mathcal{T}}$ denote the fully-discrete and the iterative solutions due to (18) and (32)–(31), respectively. Let*

$$e_{\underline{\sigma}}^i := \underline{\sigma}^i - \underline{\sigma}, \quad e_p^i := p^i - p, \quad e_{\mathbf{w}}^i := \mathbf{w}^i - \mathbf{w}, \quad e_{\mathbf{u}}^i := \mathbf{u}^i - \mathbf{u}, \quad e_{\boldsymbol{\xi}}^i := \boldsymbol{\xi}^i - \boldsymbol{\xi} \quad (33)$$

denote the respective error quantities. Then for $\beta \leq \frac{1}{2} \frac{d\alpha^2}{2\mu + d\lambda}$ it holds

$$\left(2c_0 + 2C_P \alpha_w \Delta t + \frac{d\alpha^2}{2\mu + d\lambda} - \beta \right) \|e_p^i\|^2 \leq \left(\frac{d\alpha^2}{2\mu + d\lambda} - \beta \right) \|e_p^{i-1}\|^2,$$

where C_P denotes a Poincaré constant, and α_w is a lower bound on the inverse of the permeability $\boldsymbol{\kappa}$. Thus, the fixed-stress split converges, and the predicted convergence is optimized for the destabilization parameter $\beta = \frac{1}{2} \frac{d\alpha^2}{2\mu + d\lambda}$.

Proof. Let $\beta \geq 0$ (to be specified later). Taking the difference between (31)–(32) and (18), the error quantity $(e_{\underline{\sigma}}^i, e_p^i, e_{\mathbf{w}}^i, e_{\mathbf{u}}^i, e_{\boldsymbol{\xi}}^i) \in \mathbf{X}_{\mathcal{T}}$ satisfies the error equations

$$\mathcal{A}_{\underline{\sigma}}(e_{\underline{\sigma}}^i, \boldsymbol{\tau}) + \tilde{\alpha}(e_p^i, \operatorname{tr}(\boldsymbol{\tau})) + (e_{\mathbf{u}}^i, \operatorname{div} \boldsymbol{\tau}) + (e_{\boldsymbol{\xi}}^i \cdot \boldsymbol{\chi}, \boldsymbol{\tau}) = 0 \quad (34a)$$

$$\tilde{\alpha}(\operatorname{tr} e_{\underline{\sigma}}^{i-1}, q) + \mathcal{A}_p(e_p^i, q) - \beta(e_p^i - e_p^{i-1}, q) + (\operatorname{div} e_{\mathbf{w}}^i, q) = 0 \quad (34b)$$

$$(\operatorname{div} e_{\underline{\sigma}}^i, \mathbf{v}) = 0 \quad (34c)$$

$$(e_{\underline{\sigma}}^i, \boldsymbol{\eta} \cdot \boldsymbol{\chi}) = 0 \quad (34d)$$

$$(e_p^i, \operatorname{div} \mathbf{z}) - \frac{1}{\Delta t} \mathcal{A}_{\tilde{\mathbf{w}}}(e_{\mathbf{w}}^i, \mathbf{z}) = 0 \quad (34e)$$

for all $(\boldsymbol{\tau}, q, \mathbf{z}, \mathbf{v}, \boldsymbol{\eta}) \in \mathbf{X}_{\mathcal{T}}$. To eliminate all coupling terms in (34), we test (34a) with $\boldsymbol{\tau} = -e_{\underline{\sigma}}^{i-1}$, (34b) with $q = e_p^i$, (34c) at iteration $i - 1$ with $\mathbf{v} = e_{\mathbf{u}}^i$, (34d) at iteration $i - 1$ with $\boldsymbol{\eta} = e_{\boldsymbol{\xi}}^i$, and (34e) with $\mathbf{z} = -e_{\mathbf{w}}^i$ and obtain

$$-\mathcal{A}_{\underline{\sigma}}(e_{\underline{\sigma}}^i, e_{\underline{\sigma}}^{i-1}) + \mathcal{A}_p(e_p^i, e_p^i) + \frac{1}{\Delta t} \mathcal{A}_{\tilde{\mathbf{w}}}(e_{\mathbf{w}}^i, e_{\mathbf{w}}^i) - \beta(e_p^i - e_p^{i-1}, e_p^i) = 0. \quad (35)$$

To simplify the expression, we reduce the flux term to a pressure term by employing a Poincaré inequality-type argument for mixed flow problems, cf., e.g., [15] in the context of poromechanics, and obtain (introducing a Poincaré constant C_P , a lower bound on the inverse of the permeability α_w and for convenience a summarizing, effective constant $C = C(\mu, \lambda, c_0, \alpha_w, C_P, \Delta t)$, where we recall the rescaling $\mathbf{w} = \Delta t \hat{\mathbf{w}}$)

$$\mathcal{A}_p(e_p^i, e_p^i) + \frac{1}{\Delta t} \mathcal{A}_{\hat{\mathbf{w}}}(e_{\hat{\mathbf{w}}}^i, e_{\hat{\mathbf{w}}}^i) \geq (\tilde{c}_0 + C_P \alpha_w \Delta t) \|e_p^i\|^2 =: \left(\frac{d\alpha^2}{2\mu + d\lambda} + C \right) \|e_p^i\|^2. \quad (36)$$

We split and reorganize the pressure terms, such that in summary, it holds

$$C \|e_p^i\|^2 + \left(\frac{d\alpha^2}{2\mu + d\lambda} - \beta \right) (e_p^i - e_p^{i-1}, e_p^i) + \frac{d\alpha^2}{2\mu + d\lambda} (e_p^i, e_p^{i-1}) - \mathcal{A}_{\underline{\sigma}}(e_{\underline{\sigma}}^i, e_{\underline{\sigma}}^{i-1}) \leq 0. \quad (37)$$

We aim to make use of the binomial and polarization identities

$$(a - b)a = \frac{1}{2}a^2 + \frac{1}{2}(a - b)^2 - \frac{1}{2}b^2, \quad ab = \frac{1}{4}(a + b)^2 - \frac{1}{4}(a - b)^2 \quad (38)$$

for placeholders a and b , which also extent to general bilinear forms. Application to (37) yields

$$\begin{aligned} & \left(C + \frac{1}{2} \left(\frac{d\alpha^2}{2\mu + d\lambda} - \beta \right) \right) \|e_p^i\|^2 + \frac{1}{4} \left(\frac{d\alpha^2}{2\mu + d\lambda} - 2\beta \right) \|e_p^i - e_p^{i-1}\|^2 + \frac{1}{4} \mathcal{A}_{\underline{\sigma}}(e_{\underline{\sigma}}^i - e_{\underline{\sigma}}^{i-1}, e_{\underline{\sigma}}^i - e_{\underline{\sigma}}^{i-1}) \\ & + \frac{1}{4} \frac{d\alpha^2}{2\mu + d\lambda} \|e_p^i + e_p^{i-1}\|^2 - \frac{1}{4} \mathcal{A}_{\underline{\sigma}}(e_{\underline{\sigma}}^i + e_{\underline{\sigma}}^{i-1}, e_{\underline{\sigma}}^i + e_{\underline{\sigma}}^{i-1}) \\ & \leq \frac{1}{2} \left(\frac{d\alpha^2}{2\mu + d\lambda} - \beta \right) \|e_p^{i-1}\|^2. \end{aligned} \quad (39)$$

From (34a), summed for iterations i and $i - 1$ and tested with $\underline{\tau} = e_{\underline{\sigma}}^i + e_{\underline{\sigma}}^{i-1}$, utilizing (34c)–(34c) to drop coupling terms, and the definition of $\tilde{\alpha} = \frac{\alpha}{2\mu + d\lambda}$, we obtain

$$\mathcal{A}_{\underline{\sigma}}(e_{\underline{\sigma}}^i + e_{\underline{\sigma}}^{i-1}, e_{\underline{\sigma}}^i + e_{\underline{\sigma}}^{i-1}) = -\tilde{\alpha} \left(e_p^i + e_p^{i-1}, \text{tr}(e_{\underline{\sigma}}^i + e_{\underline{\sigma}}^{i-1}) \right) \leq \frac{\sqrt{d}\alpha}{\sqrt{2\mu + d\lambda}} \|e_p^i + e_p^{i-1}\| \mathcal{A}_{\underline{\sigma}}(e_{\underline{\sigma}}^i + e_{\underline{\sigma}}^{i-1}, e_{\underline{\sigma}}^i + e_{\underline{\sigma}}^{i-1})^{1/2}, \quad (40)$$

where the inequality follows from the Cauchy-Schwarz inequality and a standard (pointwise) AM-QM inequality

$$\mathcal{A}_{\underline{\sigma}}(\underline{\tau}, \underline{\tau}) = \frac{1}{2\mu} (\underline{\tau}, \underline{\tau}) - \frac{1}{2\mu} \frac{\lambda}{2\mu + d\lambda} (\text{tr}(\underline{\tau}), \text{tr}(\underline{\tau})) \geq \frac{1}{d} \frac{1}{2\mu + d\lambda} (\text{tr}(\underline{\tau}), \text{tr}(\underline{\tau})). \quad (41)$$

Finally, under the condition $\beta \leq \frac{1}{2} \frac{d\alpha^2}{2\mu + d\lambda}$, we can drop various non-negative terms in (39) and it remains

$$\left(C + \frac{1}{2} \left(\frac{d\alpha^2}{2\mu + d\lambda} - \beta \right) \right) \|e_p^i\|^2 \leq \frac{1}{2} \left(\frac{d\alpha^2}{2\mu + d\lambda} - \beta \right) \|e_p^{i-1}\|^2.$$

This concludes the proof. \square

Remark 3 (Convergence of all fields). *For $\beta \leq \frac{1}{2} \frac{d\alpha^2}{2\mu + d\lambda}$, an argument based on an inequality of the type (40) results in direct convergence of the stress error $e_{\underline{\sigma}}^i$. Inf-sup stability of the mechanics subproblem results in convergence of the errors $(e_{\mathbf{u}}^i, e_{\underline{\xi}}^i)$, while the overall inf-sup stability of the fully-mixed formulation yields convergence of the flux error $e_{\mathbf{w}}^i$.*

Remark 4 (Theoretically vs. practically optimal tuning). *As discussed in other works on optimizing the stabilization [12, 33, 34], the practically optimal tuning depends on further factors including separation of boundaries into Dirichlet and Neumann boundaries as well as the overall physical character of the solution, stability constants as inf-sup constant etc. The theoretical optimum suggested by the theory should therefore be foremost understood as maximal destabilization with remaining guaranteed robustness.*

Remark 5 (Extension to non-trivial boundary conditions). *The splitting strategy and its theoretical analysis in Lemma 3 are independent of any chosen boundary conditions. As the analysis is essentially considering the error equations (34), all right hand sides (also those that would be introduced as surface integrals weakly encoding boundary conditions) cancel and all functions involved are error terms canceling any strongly encoded boundary conditions, reducing the discussions – as above – to function spaces with zero traces. Overall, the convergence rate and deduction of a tuned (de-)stabilization parameter holds in general.*

6 Numerical results

We consider two numerical examples in two dimensions to verify our theory. Both examples are designed to have an analytical solution allowing for assessing the spatial approximation properties. In addition, by varying material parameters, the problem has either a loosely or tightly coupling which enables a fair assessment of the performance of iterative splitting methods, its dependence on material parameters and the potential of improving it through destabilization. The first example is using Example 8.1 in [3] and is based on a manufactured solution, while the second example is the classical Mandel problem, cf., e.g., [23]. For the spatial discretization, we use Raviart–Thomas spaces of order k for the Darcy velocity and for each row of the total stress, discontinuous piecewise polynomials of degree k for the scalar pressure, discontinuous vector-valued piecewise polynomials of degree k for the displacement, and continuous piecewise polynomials of degree k for the rotation, with $k \geq 1$. All computations were carried out in Python using the finite element library `NGSolve/Netgen` for the spatial discretization and assembly of the discrete systems [31]. Auxiliary tasks, including array handling, sparse matrix operations, and root finding for the analytical Mandel solution, were implemented using `NumPy` and `SciPy` [20, 35].

6.1 Manufactured solution on the unit square

We consider on the unit square $\Omega = [0, 1]^2$ the manufactured polynomial solution

$$\mathbf{u}(\mathbf{x}, t) := \begin{pmatrix} tx(1-x)y(1-y) \\ ty(1-y)x(1-x) \end{pmatrix}, \quad p(\mathbf{x}, t) := tx(1-x)y(1-y), \quad 0 \leq t \leq 1. \quad (42)$$

The source terms, initial conditions, and Dirichlet boundary conditions are chosen such that (42) is the exact solution of the continuous Biot system in strong form, cf. section 2.

To systematically investigate the effect of the coupling strength and assess the robustness with respect to key parameters (related to compressibility and permeability), we reduce the overall parameter dependence to two scaling parameters. More precisely, we choose

$$\boldsymbol{\kappa} = \frac{\gamma_1}{\gamma_2} \mathbf{I}, \quad c_0 = \gamma_1, \quad \alpha = 1, \quad \mu = 0.6, \quad \lambda = 0.6 \gamma_2.$$

Here, γ_1 mainly scales the storage coefficient and the permeability and thus the critical coupling strength between flow and mechanics, cf. convergence rate in Lemma 3,

$$\tau = \frac{\alpha^2}{c_0(2\mu + 2\lambda)}.$$

Small values of τ correspond to weak coupling, whereas large values of τ correspond to strongly coupled regimes. Additionally, γ_2 controls the Lamé parameter λ and permeability κ and thus influences how compressible and permeable the solid skeleton is. In the experiments below, we vary

$$\gamma_1 \in \{10^{-3}, 10^{-2}, 10^{-1}, 1, 10\}, \quad \gamma_2 \in \{10^{-2}, 10^{-1}, 1, 10, 10^2, 10^3, 10^4\},$$

and we consider polynomial orders $k = 1, 2, 3$. This allows us to examine both the approximation properties of the method and the dependence of the iterative solver on the discretization order.

For the iterative solver, we compare two splitting schemes, namely the classical fixed-stress split ($\beta = 0$) and the tuned fixed-stress split ($\beta = \frac{1}{2} \frac{d\alpha^2}{2\mu + d\lambda}$) suggested by the theory, cf. Theorem 3. At each time step, the splitting iteration is terminated once the relative change between two successive iterates is below a prescribed tolerance for both subproblems. More precisely, denoting by

$$X_f^m := (\mathbf{w}_h^m, p_h^m), \quad X_m^m := (\boldsymbol{\sigma}_h^m, \mathbf{u}_h^m, \boldsymbol{\xi}_h^m)$$

the flow and mechanics iterates at iteration m , respectively, we stop as soon as

$$\frac{\|X_f^m - X_f^{m-1}\|_2}{\|X_f^{m-1}\|_2 + \varepsilon_0} \leq \text{tol} \quad \text{and} \quad \frac{\|X_m^m - X_m^{m-1}\|_2}{\|X_m^{m-1}\|_2 + \varepsilon_0} \leq \text{tol}, \quad (43)$$

where $\text{tol} = 10^{-6}$ and $\varepsilon_0 = 10^{-14}$ is a small safeguard parameter. Thus, (43) measures the relative update between successive fixed-point iterates rather than the algebraic residual of the monolithic coupled system.

For all computations, the unit square is discretized by a structured triangulation obtained from an $N \times N$ subdivision, so that the mesh size satisfies $h \sim N^{-1}$. In the iteration-count experiments, we keep the spatial and temporal discretizations fixed and choose $N = 16$ and $\Delta t = 1/4$ on the time interval $[0, 1]$. In the convergence study, we use the same time interval and time step, but successively refine the mesh and evaluate the spatial approximation errors at the final time $t = 1$.

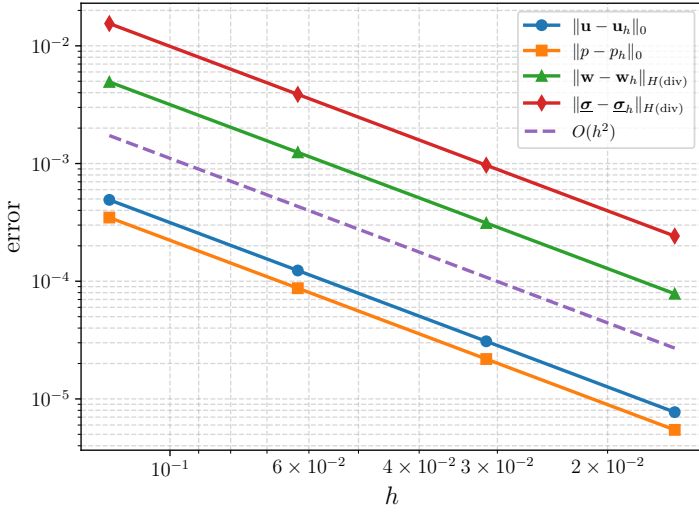
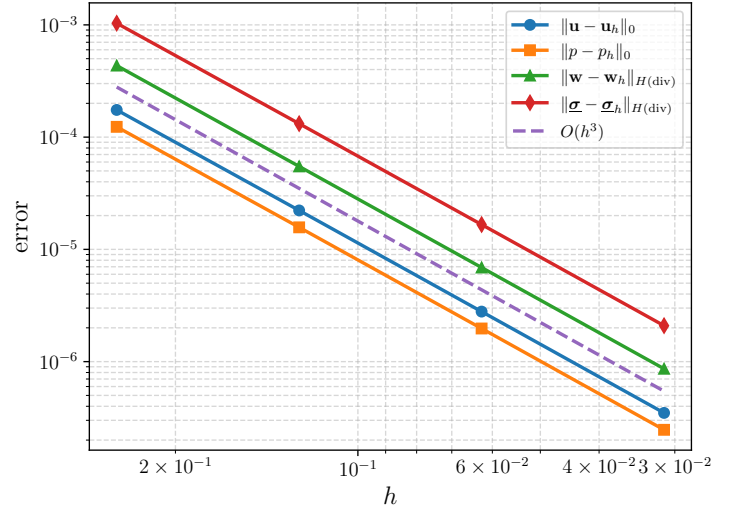
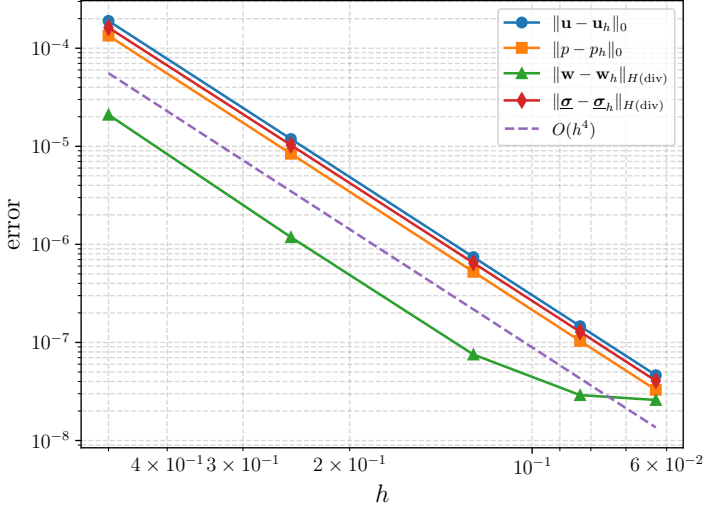
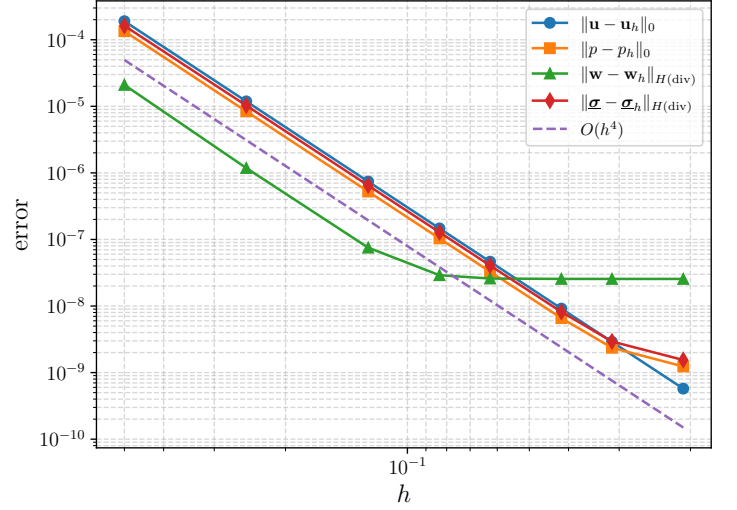
(a) $k = 1$ (b) $k = 2$ (c) $k = 3$ (d) $k = 3$, further mesh refinement

Figure 1: Spatial convergence for the manufactured solution with $\gamma_1 = \gamma_2 = 1$ and $\beta = 0$. The errors are evaluated at the final time $t = 1$ for discrete space orders $k = 1, 2, 3$.

We first examine the spatial approximation behavior for the reference choice $\gamma_1 = \gamma_2 = 1$ without tuning, that is, with $\beta = 0$. The convergence results are displayed in Figure 1.

For $k = 1$ and $k = 2$, the observed decay is consistent with approximately $\mathcal{O}(h^{k+1})$ for all primary variables. For $k = 3$, the same convergence behavior can be observed on the coarser mesh sequence. For finer meshes, some of the error curves no longer decrease with the expected rate. This is due to other error contributions, such as the fixed stopping tolerance in the splitting iteration and floating-point effects, and not to a loss of consistency of the discretization; ideally, tolerances for stopping criteria are correlated with discretization errors [21]. Overall, the figure confirms the expected optimal convergence behavior of the mixed method for displacement, pressure, velocity, and total stress.

We next turn to the iterative behavior of the splitting scheme and report the average number of iterations per time step required to satisfy (43). Table 1 shows the results obtained by varying γ_1 while keeping $\gamma_2 = 1$. Since in this case decreasing γ_1 decreases both the storage coefficient c_0 and the permeability scale, the coupling strength τ increases substantially. The iteration counts reflect this trend very clearly: the problem moves from a weakly coupled regime, where both schemes converge in only a few iterations, to a strongly coupled regime, where the untuned splitting becomes significantly more expensive. For this case, the benefit of tuning becomes more pronounced as the coupling becomes stronger. In particular, for $\gamma_1 = 10^{-3}$ the average number

of iterations is reduced from about 180 to about 96 by the tuned scheme.

A complementary picture is obtained by varying γ_2 while keeping $\gamma_1 = 1$, see Table 2. Here, increasing γ_2 increases the Lamé parameter λ , and therefore drives the mechanics toward the nearly incompressible regime, with Poisson ratio approaching 1/2. At the same time, since $\kappa = \gamma_1/\gamma_2 \mathbf{I}$, large values of γ_2 also decrease the permeability. In terms of the coupling strength τ , larger γ_2 correspond to weaker coupling, and the iteration counts indeed become very small in this regime. For smaller values of γ_2 , the coupling strength increases toward and beyond $\tau \approx 1$, and the tuned scheme again yields a systematic reduction of the iteration counts.

At the same time, the large- γ_2 regime should be interpreted with some care. The manufactured solution (42) remains an exact solution for all parameter choices by construction, so the test is mathematically fully valid throughout. However, for very large γ_2 it becomes less representative of the characteristic behavior of a genuinely nearly incompressible poroelastic response, since the spatial and temporal profiles of \mathbf{w} and p are fixed a priori while the material coefficients are varied over several orders of magnitude. In that sense, the example is best viewed as a controlled benchmark for discretization and iteration rather than as a physically realistic model in the extreme nearly incompressible limit.

This observation is also relevant when interpreting the velocity errors. In the large- γ_2 regime, the permeability is very small, so the Darcy velocity itself becomes small in magnitude, while its divergence must still balance the mass conservation constraint. In such a setting, accurate control of the $H(\text{div})$ -error of the velocity can become more delicate, especially for a manufactured solution that is not specifically tailored to this singularly perturbed regime. Thus, a deterioration in the $H(\text{div})$ -velocity error for very large γ_2 should not necessarily be interpreted as a structural deficiency of the method, but rather as a consequence of combining an extreme parameter regime with a fixed manufactured solution.

γ_1	coupling strength	$k = 1$		$k = 2$		$k = 3$	
		off	tuned	off	tuned	off	tuned
10	8.333×10^{-2}	4.25	4.00	4.25	4.00	4.25	4.00
1	8.333×10^{-1}	7.25	6.00	7.25	6.00	7.25	6.00
0.1	8.333×10^0	18.75	11.50	18.75	11.50	18.75	11.50
0.01	8.333×10^1	60.50	33.00	60.50	33.00	60.50	33.00
0.001	8.333×10^2	182.50	98.50	178.50	96.25	178.50	96.25

Table 1: Average number of iterations per time step for varying γ_1 with fixed $\gamma_2 = 1$.

γ_2	Poisson ratio	coupling strength	$k = 1$		$k = 2$		$k = 3$	
			off	tuned	off	tuned	off	tuned
10000	0.49995	1.667×10^{-4}	3.00	4.00	3.00	4.00	3.00	4.00
1000	0.4995	1.665×10^{-3}	4.00	4.50	4.00	4.50	4.00	4.50
100	0.49505	1.650×10^{-2}	4.50	5.25	4.50	5.25	4.50	5.25
10	0.45455	1.515×10^{-1}	6.25	6.00	6.25	6.00	6.25	6.00
1	0.25	8.333×10^{-1}	7.25	6.00	7.25	6.00	7.25	6.00
0.1	0.04545	1.515×10^0	5.00	4.25	5.00	4.25	5.00	4.25
0.01	0.00495	1.650×10^0	4.00	3.50	4.00	3.50	4.00	3.50

Table 2: Average number of iterations per time step for varying γ_2 with fixed $\gamma_1 = 1$.

A further important observation in both Tables 1 and 2 is that the iteration counts are nearly identical for $k = 1, 2, 3$. Hence, for this example, the convergence of the splitting iteration is governed primarily by the physical parameters and the coupling strength, whereas the polynomial degree mainly affects the spatial accuracy of the discrete solution. This separation is favorable in practice: one may increase the approximation order to improve accuracy without significantly affecting the convergence of the iterative coupling scheme.

In summary, the experiments confirm two main points. First, the proposed discretization exhibits the expected spatial convergence behavior for all primary variables. Second, the tuning parameter in the splitting scheme is particularly beneficial in strongly coupled regimes, where it leads to a substantial reduction in iteration counts, while in weakly coupled regimes both variants

perform comparably. Moreover, no significant difference across discretizations is encountered in line with the convergence result in Lemma 3, which is agnostic to the spatial discretization.

6.2 Mandel's problem

Mandel's problem is a classical benchmark in poroelasticity for assessing how accurately a numerical method captures the coupling between elastic deformation and pore-pressure diffusion. It is particularly well known for the non-monotonic evolution of the pore pressure near the center of the specimen. In this study, we consider a rectangular fluid-saturated poroelastic sample of width $2a$ and height $2b$, subjected to an instantaneous compressive load through rigid plates attached to the top and bottom boundaries. The lateral boundaries are drained, and gravitational effects are neglected. Owing to the availability of exact analytical expressions for the pressure, displacement, Darcy velocity, and stress fields, this benchmark is widely used for the validation of coupled hydro-mechanical models.

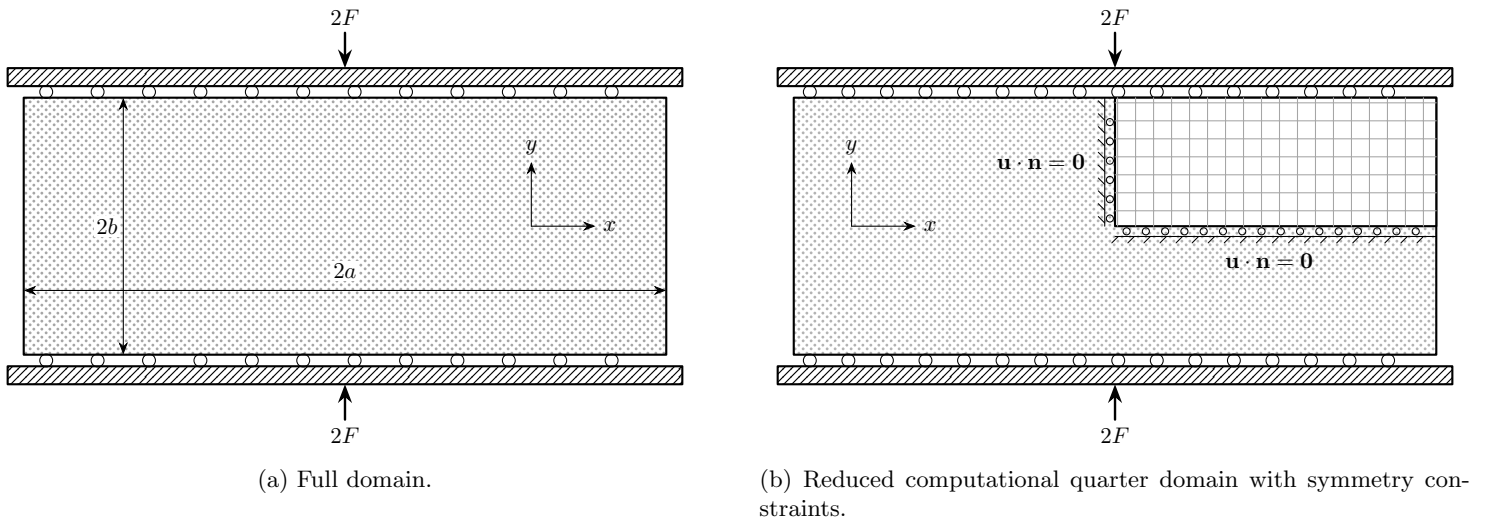


Figure 2: Schematic illustration of Mandel's problem and the reduced computational quarter domain used in the simulations.

We consider the classical Mandel benchmark problem; see, for example, [23]. Owing to symmetry, the problem is solved on the quarter domain $\Omega = (0, a) \times (0, b)$. In our computations, we prescribe the following initial conditions:

$$\begin{aligned}
 p(x, 0) &= \frac{FB(1 + \nu_u)}{3a}, & x \in (0, a), \\
 \underline{\sigma}_{11}(x, 0) &= \underline{\sigma}_{12}(x, 0) = \underline{\sigma}_{21}(x, 0) = 0, & x \in (0, a), \\
 \underline{\sigma}_{22}(x, 0) &= -\frac{F}{a}, & x \in (0, a).
 \end{aligned} \tag{44}$$

and the boundary conditions

$$\begin{aligned}
 p &= 0, & \underline{\sigma} \cdot \mathbf{n} &= 0, & \text{on } x &= a, \\
 \mathbf{w} \cdot \mathbf{n} &= 0, & \mathbf{u} \cdot \mathbf{n} &= u_2^{\text{analytical}}(b, t), & \underline{\sigma}_{12} &= 0, & \text{on } y &= b, \\
 \mathbf{w} \cdot \mathbf{n} &= 0, & \mathbf{u} \cdot \mathbf{n} &= 0, & \underline{\sigma}_{21} &= 0, & \text{on } x &= 0, \\
 \mathbf{w} \cdot \mathbf{n} &= 0, & \mathbf{u} \cdot \mathbf{n} &= 0, & \underline{\sigma}_{12} &= 0, & \text{on } y &= 0.
 \end{aligned} \tag{45}$$

This benchmark admits an exact series solution satisfying the above conditions; see [1]. In the notation adopted in this paper,

the exact pressure and displacement are given by

$$p(x, t) = \frac{2FB(1 + \nu_u)}{3a} \sum_{n=1}^{\infty} \frac{\sin(\alpha_n)}{\alpha_n - \sin(\alpha_n) \cos(\alpha_n)} \left(\cos\left(\frac{\alpha_n x}{a}\right) - \cos(\alpha_n) \right) e^{-\frac{\alpha_n^2 ct}{a^2}},$$

$$\mathbf{u}_1(x, t) = \left[\frac{F\nu}{2\mu a} - \frac{F\nu_u}{\mu a} \sum_{n=1}^{\infty} \frac{\sin(\alpha_n) \cos(\alpha_n)}{\alpha_n - \sin(\alpha_n) \cos(\alpha_n)} e^{-\frac{\alpha_n^2 ct}{a^2}} \right] x + \frac{F}{\mu} \sum_{n=1}^{\infty} \frac{\cos(\alpha_n)}{\alpha_n - \sin(\alpha_n) \cos(\alpha_n)} \sin\left(\frac{\alpha_n x}{a}\right) e^{-\frac{\alpha_n^2 ct}{a^2}},$$

$$\mathbf{u}_2(y, t) = \left[-\frac{F(1 - \nu)}{2\mu a} + \frac{F(1 - \nu_u)}{\mu a} \sum_{n=1}^{\infty} \frac{\sin(\alpha_n) \cos(\alpha_n)}{\alpha_n - \sin(\alpha_n) \cos(\alpha_n)} e^{-\frac{\alpha_n^2 ct}{a^2}} \right] y,$$

while Darcy velocity and total stress reads

$$\underline{\boldsymbol{\sigma}}_{11} = \underline{\boldsymbol{\sigma}}_{12} = \underline{\boldsymbol{\sigma}}_{21} = 0,$$

$$\underline{\boldsymbol{\sigma}}_{22}(x, t) = -\frac{F}{a} - \frac{2F}{a} \sum_{n=1}^{\infty} \frac{\sin(\alpha_n)}{\alpha_n - \sin(\alpha_n) \cos(\alpha_n)} \left[\frac{\nu_u - \nu}{1 - \nu} \cos\left(\frac{\alpha_n x}{a}\right) - \cos(\alpha_n) \right] e^{-\frac{\alpha_n^2 ct}{a^2}},$$

$$\mathbf{w}_1(x, t) = \frac{2FB(1 + \nu_u)k}{3a^2\eta} \sum_{n=1}^{\infty} \frac{\alpha_n \sin(\alpha_n)}{\alpha_n - \sin(\alpha_n) \cos(\alpha_n)} \sin\left(\frac{\alpha_n x}{a}\right) e^{-\frac{\alpha_n^2 ct}{a^2}},$$

$$\mathbf{w}_2(x, t) = 0.$$

Here, α_n denotes the positive roots of the transcendental equation

$$\tan(\alpha_n) = \frac{1 - \nu}{\nu_u - \nu} \alpha_n, \quad n \in \mathbb{N}. \quad (46)$$

The quantities ν , F , B , c , and a denote the benchmark parameters appearing in the closed-form solution. In our computations, their values are determined from the physical Biot parameters listed in Table 3.

Table 3: Input parameters for Mandel's problem

Symbol	Quantity	Value
a	Dimension in x	100 m
b	Dimension in y	10 m
E	Young's modulus	5.94×10^9 Pa
ν	Poisson's ratio	0.2
c_f	Fluid compressibility	3.03×10^{-10} /Pa
F	Applied load	6.0×10^8 N m ⁻¹
α	Biot's constant	1.0
k	Permeability	100 mD
ϕ	Initial porosity	0.2
η	Fluid viscosity	1.0 cP
Δx	Grid spacing in x	2.5 m
Δy	Grid spacing in y	0.25 m
Δt	Time step size	10 s
t_T	Total simulation time	50,000 s
B	Skempton coefficient	0.83333
ν_u	Undrained Poisson's ratio	0.44
M	Biot's modulus	1.65×10^{10} Pa
c	Diffusivity coefficient	0.465 m ² s ⁻¹

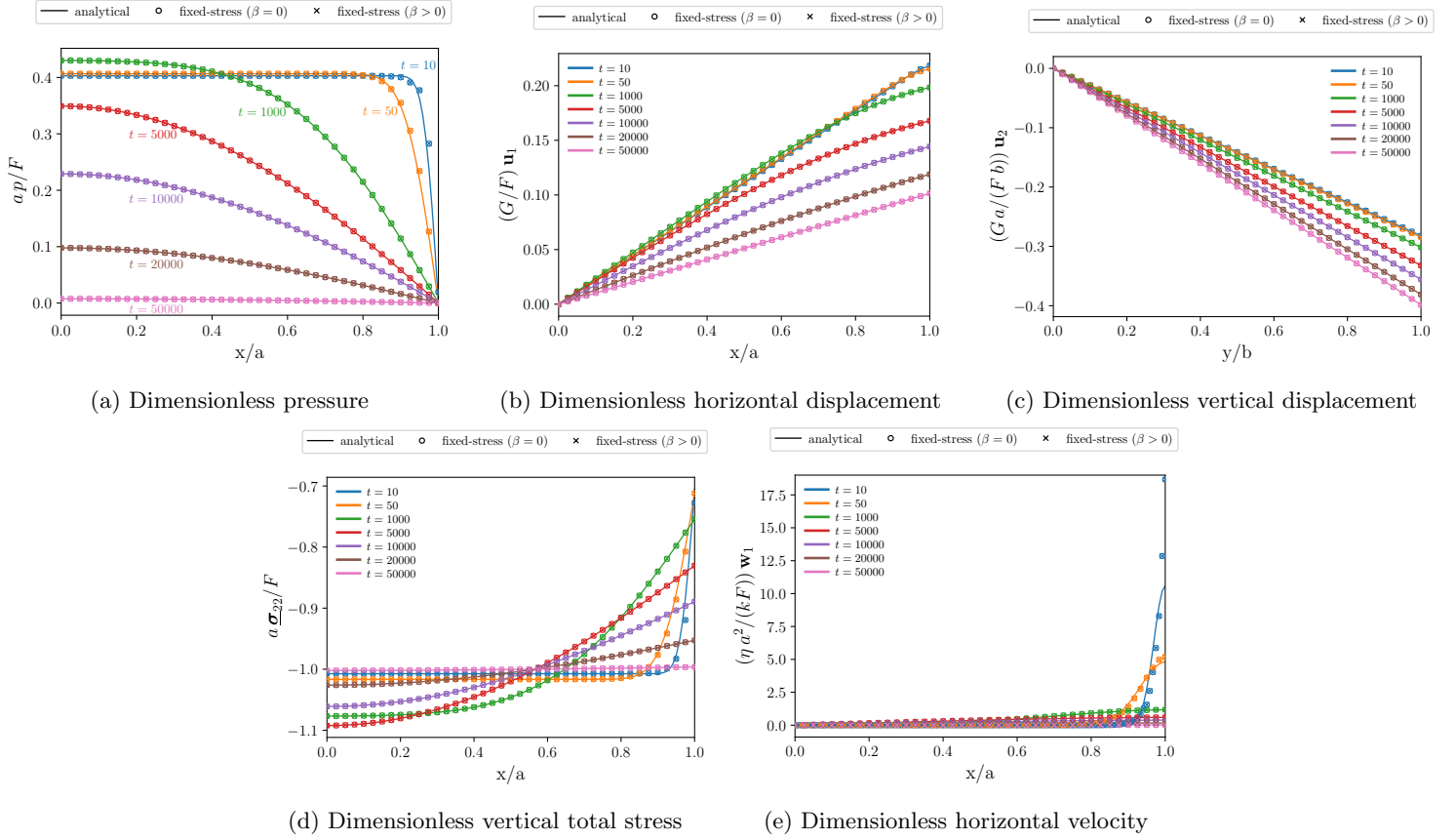


Figure 3: Dimensionless solution variables for Mandel's problem.

For the numerical simulation of Mandel's problem shown in Figure 3, we use the parameter set listed in Table 3, the lowest discrete space order choice $k = 1$, a structured anisotropic mesh with $\Delta x = 2.5$ and $\Delta y = 0.25$, and a uniform time step $\Delta t = 10$ on the interval $[0, 50000]$. We compare the untuned fixed-stress splitting, corresponding to $\beta = 0$, with the tuned variant using the theoretically motivated choice of $\beta = \frac{1}{2} \frac{d\alpha^2}{2\mu + d\lambda}$. In addition, we test a tuning value motivated by Remark 4 and the fact that Mandel's problem has a specific one-dimensional character, in particular in the expected stress regime, cf. the analytical solution for $\underline{\sigma}$ being nonzero only for a single entry. This motivates to employ a tuning parameter $\beta = \beta^{1D}$, which reduces the effective linearization to a one-dimensional setting

$$\frac{d\alpha^2}{2\mu + d\lambda} - \beta^{1D} \stackrel{!}{=} \frac{\alpha^2}{2\mu + \lambda} \quad \Leftrightarrow \quad \beta^{1D} = \frac{\alpha^2 \cdot 2\mu(d-1)}{(2\mu + d\lambda)(2\mu + \lambda)}.$$

We consider this additional tuning value and refer to it as *1D-tuned*.

At the same time, this benchmark supports the statements made in Remark 4. In particular, it illustrates that the theoretically optimized destabilization does not need to be practically optimal. The 1D-tuned variant requires 3.0 iterations on average for each time step, compared with 6.0402 and 6.0072 for the standard and theoretically tuned variants, respectively. Moreover, we observe that theoretical tuning does not necessarily lead to improved performance in practice. This, however, should be interpreted in light of the fact that Mandel's problem, despite being posed in two dimensions, exhibits a strongly one-dimensional character. Figure 3 shows the numerical and analytical solutions for the dimensionless pressure, displacements, vertical stress, and horizontal Darcy velocity at several time instances. Overall, the agreement is very good for all quantities. In particular, both splitting variants reproduce the analytical solution with essentially indistinguishable profiles, which indicates that the spatial discretization error dominates the remaining algebraic error.

The pressure plot in Figure 3(a) shows the characteristic behavior of Mandel's problem. At early times the pressure is largest in the interior and vanishes at the drained boundary $x = a$. As time evolves, the pressure near the center remains elevated for some time before eventually decaying, reflecting the classical Mandel effect. The displacement plots in Figures 3(b)–(c) are also consistent with the expected mechanics: the horizontal displacement increases with x , while the vertical displacement is

compressive and varies essentially linearly in the vertical direction. Likewise, the vertical total stress in Figure 3(d) starts from the nearly uniform initial state and then develops the expected spatial variation induced by the coupled drainage process. The largest visible discrepancy occurs in the horizontal Darcy velocity near the drained boundary $x = a$ at early times; see Figure 3(e). This is not unexpected. The discrete velocity is approximated in an $H(\text{div})$ -conforming Raviart–Thomas space, for which the natural control is in terms of fluxes, moments, and divergence, rather than pointwise values. Therefore, near a boundary layer or steep spatial variation, pointwise plots of the velocity may show an overshoot even when the integral behavior of the discrete flux is well captured.

In summary, this benchmark confirms that the proposed method reproduces the analytical Mandel solution accurately for all primary variables. For the parameter range considered here, the fixed-stress splitting converges reliably for all three choices of tuning. While the theoretically tuned parameter has only a minor influence on the iteration count compared with the untuned scheme, the additional 1D-tuned choice leads to a substantial reduction in the number of iterations. This is consistent with the strongly one-dimensional character of Mandel’s problem.

As a final numerical experiment, we investigate how the performance of the splitting scheme changes when the Young’s modulus and the applied load are scaled simultaneously. More precisely, we set

$$E = \gamma_3 E_{\text{ref}}, \quad F = \gamma_3 F_{\text{ref}},$$

with

$$E_{\text{ref}} = 5.94 \times 10^9, \quad F_{\text{ref}} = 6.0 \times 10^8,$$

while updating all model parameters depending on E accordingly and keeping the remaining benchmark parameters fixed. This scaling keeps the solution variables on a broadly comparable scale across the different tests, while the coupling strength changes. The corresponding average numbers of iterations per time step are reported in Table 4.

γ_3	coupling strength	$k = 1$			$k = 2$			$k = 3$		
		off	tuned	1D-tuned	off	tuned	1D-tuned	off	tuned	1D-tuned
10^2	5×10^{-2}	4.0	3.5	3.0	4.0	3.5	3.0	4.0	3.5	3.0
10^1	5×10^{-1}	5.8	5.0	3.0	5.8	5.0	3.0	5.8	5.0	3.0
10^0	5×10^0	9.0	7.1	3.0	9.0	7.1	3.0	9.0	7.1	3.0
10^{-1}	5×10^1	9.6	8.1	4.4	9.6	8.0	3.3	9.6	8.0	3.1
10^{-2}	5×10^2	9.2	18.8	8.1	9.3	11.9	6.5	9.4	7.9	5.0
10^{-3}	5×10^3	9.1	121.1	14.3	9.2	54.9	11.9	9.1	32.1	11.1

Table 4: Average number of iterations per time step for varying $\gamma_3 = E/E_{\text{ref}} = F/F_{\text{ref}}$, comparing off, tuned, and 1D-tuned configurations.

The results show that for weakly and moderately coupled regimes, that is, for $\gamma_3 = 100, 10, 1$, the theoretically tuned scheme is consistently more efficient than the untuned one. In these cases, the average iteration count is reduced from 4.00 to 3.50, from 5.80 to 5.00, and from 9.00 to 7.10, respectively. Hence, in this range the negative tuning parameter has the expected beneficial effect and improves the convergence of the fixed-stress iteration.

For smaller values of γ_3 , the coupling strength increases further. At $\gamma_3 = 10^{-1}$, the tuned scheme still gives a mild improvement, reducing the average iteration count from about 9.6 to about 8.0. However, for $\gamma_3 = 10^{-2}$ and $\gamma_3 = 10^{-3}$ the behavior changes. In these more strongly coupled regimes, the tuned scheme is no longer uniformly advantageous. For $k = 1$ and $k = 2$ the iteration counts increase substantially, and for $\gamma_3 = 10^{-3}$ this deterioration is particularly pronounced. Only for $k = 3$ does the tuned scheme remain competitive and, for the smallest values of γ_3 , outperform the untuned variant.

The performance for the additional 1D-tuned option highlights the special character of Mandel’s problem. Consistently (besides for very large coupling strength), the 1D-tuned fixed-stress split requires very few iterations and outperforms especially the theoretically tuned fixed-stress split, avoiding the deterioration for strong coupling strength. With three iterations in various cases, it confirms the physical motivation of informing the tuning based on the physical character of the expected solution, here dictated by the stress field and thus conversion from increments in volumetric stress to those in pressure. This highlights that, for the Mandel problem, the practically optimal stabilization is governed more strongly by its underlying one-dimensional character than by the theoretically optimal two-dimensional tuning parameter.

Thus, in contrast to the previous test with the manufactured solution, the present scaling reveals a more sensitive dependence of the iteration on both the coupling strength and the discretization order. In particular, once the coupling becomes sufficiently

strong, the tuned choice of β is no longer uniformly robust across all polynomial orders. The higher-order discretizations appear to handle this regime better, whereas for lower orders the same tuning may even deteriorate the convergence.

A further notable feature of Table 4 is that the untuned scheme remains relatively stable across the full range of γ_3 , with iteration counts staying close to 9 in the strongly coupled cases. By contrast, the tuned scheme shows a much stronger dependence on both γ_3 and k . This indicates that, for this scaled Mandel test, the practical effect of tuning is more delicate than in the manufactured example, and further method characteristics are impacting the convergence rate which have not been picked up in Lemma 3.

Overall, Table 4 suggests that the theoretically motivated negative tuning parameter can improve convergence in weakly and moderately coupled regimes, but its benefit is not uniform in strongly coupled regimes. In particular, for very small γ_3 the interaction between the parameter scaling, the induced coupling strength, and the spatial discretization becomes more subtle. This experiment with additional emphasis on physically motivated destabilization therefore complements the previous tests by showing that the effect of tuning can depend significantly on the underlying physical regime, consistent with previous analyses of the fixed-stress split for saddle-point formulations of the Biot equations [12]. In addition, as discussed in [33, 34], stability properties of the discretization as the inf-sup constant may impact the performance of the splitting and the optimal tuning parameter.

7 Concluding remarks

In this work, we considered the fully-mixed formulation of the Biot equations, describing two-way coupled flow and deformation in porous media. This formulation strictly enforces the conservation of mass and linear momentum. Moreover, the cross-physics coupling is symmetric which we highlight with two novel developments. We highlight the flexibility in designing families of mixed finite elements, solely requiring the stability within the single subphysics, and then resulting in overall inf-sup stability for the coupled problem. Moreover, the symmetric coupling allows for effective iterative solution by employing a naive decoupling of flow and deformation, which can be identified with the common fixed-stress split. However, in addition we theoretically show that destabilization, i.e., the application of negative (contrary to positive) stabilization, results in improved convergence, which is consistent with previous studies of the fixed-stress split for the two-field formulation reporting that the full stabilization associated with "fixing the stress" can be reduced without sacrificing performance [24, 15]. In line with previous observations, picking the optimal tuning depends on various problem characteristics [12], suggesting optimization either based informed by theory [33] or data-driven approaches [38]. Our analysis structurally differs from previous analyses of splitting schemes for symmetrically coupled problems [27, 16], opening new views on the numerical analysis of such.

Acknowledgments

JWB acknowledges support from the FRIPRO project "Unlocking maximal geological CO2 storage through experimentally validated mathematical modeling of dissolution and convective mixing (TIME4CO2)", grant nr. 355188, funded by the Research Council of Norway.

References

- [1] Y. Abousleiman, A. H.-D. Cheng, L. Cui, E. Detournay, and J.-C. Roegiers. Mandel's problem revisited. *Géotechnique*, 46(2):187–195, 1996.
- [2] Elyes Ahmed, Jan Martin Nordbotten, and Florin Adrian Radu. Adaptive asynchronous time-stepping, stopping criteria, and a posteriori error estimates for fixed-stress iterative schemes for coupled poromechanics problems. *Journal of Computational and Applied Mathematics*, 364:112312, 2020.
- [3] Elyes Ahmed, Florin Adrian Radu, and Jan Martin Nordbotten. Adaptive poromechanics computations based on a posteriori error estimates for fully mixed formulations of biot's consolidation model. *Computer Methods in Applied Mechanics and Engineering*, 347:264–294, 2019.
- [4] Ilona Ambartsumyan, Eldar Khattatov, and Ivan Yotov. A coupled multipoint stress–multipoint flux mixed finite element method for the biot system of poroelasticity. *Computer Methods in Applied Mechanics and Engineering*, 372:113407, 2020.
- [5] D.N. Arnold, R.S. Falk, and R. Winther. Mixed finite element methods for linear elasticity with weakly imposed symmetry. *Mathematics of Computation*, 76(260):1699–1723, 2007.

- [6] D.N. Arnold and R. Winther. Mixed finite elements for elasticity. *Numerische Mathematik*, 92(3):401–419, 2002.
- [7] Trygve Bærland, Jeonghun J Lee, Kent-Andre Mardal, and Ragnar Winther. Weakly imposed symmetry and robust preconditioners for biot’s consolidation model. *Computational Methods in Applied Mathematics*, 17(3):377–396, 2017.
- [8] F. Bertrand, A. Ern, and F.A. Radu. Robust and reliable finite element methods in poromechanics. *Computers and Mathematics with Applications*, 91:1–2, 2021.
- [9] M.A. Biot. General theory of three-dimensional consolidation. *Journal of Applied Physics*, 12(2):155–164, 1941.
- [10] M.A. Biot. Theory of elasticity and consolidation for a porous anisotropic solid. *Journal of Applied Physics*, 26(2):182–185, 1955.
- [11] Jakub W Both, Nicolas A Barnafi, Florin A Radu, Paolo Zunino, and Alfio Quarteroni. Iterative splitting schemes for a soft material poromechanics model. *Computer Methods in Applied Mechanics and Engineering*, 388:114183, 2022.
- [12] Jakub W Both and Uwe Köcher. Numerical investigation on the fixed-stress splitting scheme for biot’s equations: Optimality of the tuning parameter. In *European Conference on Numerical Mathematics and Advanced Applications*, pages 789–797. Springer, 2017.
- [13] Jakub Wiktor Both. On the rate of convergence of alternating minimization for non-smooth non-strongly convex optimization in banach spaces. *Optimization Letters*, 16(2):729–743, 2022.
- [14] Jakub Wiktor Both, Kundan Kumar, Jan Martin Nordbotten, and Florin Adrian Radu. The gradient flow structures of thermo-poro-visco-elastic processes in porous media. *arXiv preprint arXiv:1907.03134*, 2019.
- [15] J.W. Both, M. Borregales, J.M. Nordbotten, K. Kumar, and F.A. Radu. Robust fixed stress splitting for Biot’s equations in heterogeneous media. *Applied Mathematics Letters*, 68:101–108, 2017.
- [16] Mats Kirkesæther Brun, Thomas Wick, Inga Berre, Jan Martin Nordbotten, and Florin Adrian Radu. An iterative staggered scheme for phase field brittle fracture propagation with stabilizing parameters. *Computer Methods in Applied Mechanics and Engineering*, 361:112752, 2020.
- [17] Olivier Coussy. *Poromechanics*. John Wiley & Sons, 2004.
- [18] B. M. Fraeijs de Veubeke. Stress function approach. In *Proceedings of the World Congress on the Finite Element Method in Structural Mechanics*, Dorset, England, 1975.
- [19] Joachim Berdal Haga, Harald Osnes, and Hans Petter Langtangen. On the causes of pressure oscillations in low-permeable and low-compressible porous media. *International Journal for Numerical and Analytical Methods in Geomechanics*, 36(12):1507–1522, 2012.
- [20] Charles R. Harris, K. Jarrod Millman, Stéfan J. van der Walt, et al. Array programming with NumPy. *Nature*, 585:357–362, 2020.
- [21] Pavel Jiránek, Zdeněk Strakoš, and Martin Vohralík. A posteriori error estimates including algebraic error and stopping criteria for iterative solvers. *SIAM Journal on Scientific Computing*, 32(3):1567–1590, 2010.
- [22] Jihoon Kim, Hamdi A Tchelepi, and Ruben Juanes. Stability, accuracy, and efficiency of sequential methods for coupled flow and geomechanics. *SPE Journal*, 16(02):249–262, 2011.
- [23] Andro Mikelić, Bin Wang, and Mary F Wheeler. Numerical convergence study of iterative coupling for coupled flow and geomechanics. *Computational Geosciences*, 18(3):325–341, 2014.
- [24] Andro Mikelić and Mary F Wheeler. Convergence of iterative coupling for coupled flow and geomechanics. *Computational Geosciences*, 17(3):455–461, 2013.
- [25] M.A. Murad and A.F.D. Loula. Improved accuracy in finite element analysis of Biot’s consolidation problem. *Computer Methods in Applied Mechanics and Engineering*, 95(3):359–382, 1992.
- [26] Jan Martin Nordbotten. Stable cell-centered finite volume discretization for biot equations. *SIAM Journal on Numerical Analysis*, 54(2):942–968, 2016.

- [27] Roberto Nuca, Erlend Storvik, Florin A Radu, and Matteo Icardi. Splitting schemes for coupled differential equations: Block schur-based approaches & partial jacobi approximation. *Computers & Mathematics with Applications*, 161:190–201, 2024.
- [28] P.J. Phillips and M.F. Wheeler. A coupling of mixed and continuous Galerkin finite element methods for poroelasticity II: The discrete-in-time case. *Computational Geosciences*, 11(2):145–158, 2007.
- [29] H. Qingguo and K. Johannes. Parameter-robust stability of classical three-field formulation of Biot’s consolidation model. *Electronic Transactions on Numerical Analysis*, 48:202–226, 2018.
- [30] R. Riedlbeck, D.A. Di Pietro, A. Ern, S. Granet, and K. Kazymyrenko. Stress and flux reconstruction in Biot’s poro-elasticity problem with application to a posteriori error analysis. *Computers and Mathematics with Applications*, 73(7):1593–1610, 2017.
- [31] Joachim Schöberl. C++11 implementation of finite elements in ngsolve. Technical report, Institute of Analysis and Scientific Computing, TU Wien, Vienna, Austria, 2014.
- [32] Antonin Settari and FM Mounts. A coupled reservoir and geomechanical simulation system. *Spe Journal*, 3(03):219–226, 1998.
- [33] Erlend Storvik, Jakub W Both, Kundan Kumar, Jan M Nordbotten, and Florin A Radu. On the optimization of the fixed-stress splitting for biot’s equations. *International Journal for Numerical Methods in Engineering*, 120(2):179–194, 2019.
- [34] Erlend Storvik, Jakub Wiktor Both, Jan Martin Nordbotten, and Florin Adrian Radu. The fixed-stress splitting scheme for biot’s equations as a modified richardson iteration: Implications for optimal convergence. In *Numerical Mathematics and Advanced Applications ENUMATH 2019: European Conference, Egmond aan Zee, The Netherlands, September 30-October 4*, pages 909–917. Springer, 2020.
- [35] Pauli Virtanen, Ralf Gommers, Travis E. Oliphant, et al. SciPy 1.0: Fundamental algorithms for scientific computing in python. *Nature Methods*, 17:261–272, 2020.
- [36] Joshua A White, Nicola Castelletto, and Hamdi A Tchelepi. Block-partitioned solvers for coupled poromechanics: A unified framework. *Computer Methods in Applied Mechanics and Engineering*, 303:55–74, 2016.
- [37] S.-Y. Yi. Convergence analysis of a new mixed finite element method for Biot’s consolidation model. *Numerical Methods for Partial Differential Equations*, 30(4):1189–1210, 2014.
- [38] Yury Zabegaev, Eirik Keilegavlen, Einar Iversen, and Inga Berre. Automated linear solver selection for simulation of multiphysics processes in porous media. *Computer Methods in Applied Mechanics and Engineering*, 426:117031, 2024.